Available online at www.sciencedirect.com

ScienceDirect

Geochimica et Cosmochimica Acta 321 (2022) 311–328

Geochimica et Cosmochimica Acta

www.elsevier.com/locate/gca

Phosphate coprecipitation affects reactivity of iron (oxyhydr)oxides towards dissolved iron and sulfide

Peter Kraal [a,b,*], Case M. van Genuchten [b,c], Thilo Behrends [b]

[a] Royal Netherlands Institute for Sea Research, Department of Ocean Systems, P.O. Box 59, 1790 AB Den Burg, the Netherlands
[b] Department of Earth Sciences – Geochemistry, Faculty of Geosciences, Utrecht University, PO Box 80021, 3508 TA Utrecht, the Netherlands
[c] Department of Geochemistry, Geological Survey of Denmark and Greenland, Copenhagen, Denmark

Received 17 June 2021; accepted in revised form 29 December 2021; Available online 4 January 2022

Abstract

Iron (Fe) cycling exerts strong control on the mobility and bioavailability of the key nutrient phosphate (PO_4) in soils and sediments. Coprecipitation of PO_4 is known to alter the structure of Fe (oxyhydr)oxides (FeOx), however the environmental fate of PO_4-bearing FeOx is not well-understood. Here, PO_4-bearing FeOx with 9 mol% coprecipitated PO_4 were prepared by Fe(III) hydrolysis and Fe(II) oxidation in the presence of dissolved PO_4, in addition to pure FeOx synthesized in PO_4-free solutions. The pure and PO_4-bearing FeOx were subsequently exposed to different concentrations of dissolved Fe(II) and sulfide (2 and 10 mmol L^{-1}). Mineral transformations and the fate of PO_4 were tracked over 7–14 days with wet chemical techniques (including sequential Fe and S extraction) and synchrotron-based Fe K-edge X-ray absorption spectroscopy. Coprecipitation of PO_4 affected the rate and extent of FeOx transformation differently for Fe(II) and sulfide. Poorly-ordered PO_4-bearing FeOx was preserved in the presence of dissolved Fe(II) while pure ferrihydrite was nearly completely transformed into goethite over 7 days. By contrast, coprecipitation of PO_4 rendered FeOx more reactive towards sulfide compared to pure FeOx. Reaction with dissolved sulfide resulted in the formation of non-sulfidized Fe(II) or Fe(II) sulfide under high and low Fe/sulfide ratio, respectively. Under low Fe/sulfide ratio, Fh and PO_4-bearing, poorly-ordered FeOx were nearly completely sulfidized after 14 days. Sulfidation of FeOx led to efficient release of PO_4 into solution, and at low Fe/sulfide ratio more PO_4 was released than expected based on the extent of Fe sulfidation. The results suggest feedback mechanisms of environmental relevance: coprecipitation of strongly-sorbing species such as PO_4 disrupts FeOx structure, which affects FeOx reactivity and the overall nutrient or contaminant retention capacity of soils or sediments differently depending on the ambient redox conditions. Specifically, the switch from reducing to sulfidic conditions may be associated with the disproportionate release of nutrients and contaminants.

Keywords: Fe(II)-catalyzed transformation; Sulfidation; Ferrihydrite; Lepidocrocite; Chemical sequential extraction; X-ray absorption spectroscopy; Biogeochemical cycles; Iron redox cycling; Phosphorus retention

Abbreviations: EXAFS, extended X-ray absorption fine structure; FeOx, iron (oxyhydr)oxides; Fh, ferrihydrite; Gt, goethite; HEXS, high-energy X-ray scattering; HFO, hydrous ferric oxide; ITFA, iterative transformation factor analysis; LCF, linear combination fitting; Lp, lepidocrocite; Mag, magnetite; PDF, pair distribution function; XANES, X-ray absorption near-edge structure; XAS, X-ray absorption spectroscopy

* Corresponding author at: Royal Netherlands Institute for Sea Research, Department of Ocean Systems, P.O. Box 59, 1790 AB Den Burg, the Netherlands.
E-mail address: peter.kraal@nioz.nl (P. Kraal).

https://doi.org/10.1016/j.gca.2021.12.032
0016-7037/

1. INTRODUCTION

Phosphorus (as phosphate, PO_4) is an essential nutrient to all (aquatic) life that can cause environmental problems when it is present in high concentrations, for instance in eutrophic aquatic systems suffering from harmful algal blooms and water-quality issues (Nixon, 1995; Smith et al., 1999). In terrestrial and marine systems, PO_4 mobility and bioavailability are strongly impacted by interaction with iron (Fe) (Ruttenberg, 2014). It is one of the most abundant metals in soils and sediments and forms highly reactive minerals such as short-range-ordered and poorly crystalline Fe(III) (oxyhydr)oxides (collectively referred to here as FeOx) with a high affinity for PO_4 in oxic surface sediments (Einsele, 1936; Mortimer, 1941; Jensen et al., 1992). In the presence of dissolved Fe(II) or sulfide, reductive dissolution-precipitation mechanisms drive crystallization and sulfidation of FeOx, thereby diminishing the PO_4 retention capacity of Fe minerals and the sediment in general, and potentially triggering PO_4 release (Krom and Berner, 1980; Senn et al., 2017; Thompson et al., 2019; Queiroz et al., 2021). Reaction with excess dissolved Fe(II) can also precipitate dissolved PO_4 in the form of reduced iron phosphate minerals (Rothe et al., 2016). These processes intimately link the environmental fate of PO_4 to FeOx transformations.

Two widely-occurring FeOx with high affinity for PO_4 are ferrihydrite (Fh, $Fe(III)_{10}O_{14}(OH)_2{\cdot}nH_2O$ with $n < 1$) and lepidocrocite (Lp, γ-Fe(III)OOH) (Cornell and Schwertmann, 2003; Michel et al., 2007; Hiemstra, 2013). Ferrihydrite is a poorly-ordered, nanocrystalline Fe(III) precipitate that can form by Fe(III) hydrolysis in Fe-rich environments with strong pH gradients such as peat soils, acid sulfate soils and acid mine drainage (Ferris et al., 1989; Jambor and Dutrizac, 1998; Carlson et al., 2002; Karlsson and Persson, 2010; Queiroz et al., 2021). Ferrihydrite has an exceptionally large surface area, estimated at 300–600 $m^2\ g^{-1}$ (Poulton et al., 2004), therefore it can bind large amounts of PO_4, in excess of 2000 $\mu mol\ g^{-1}$ (Dzombak and Morel, 1990; Khare et al., 2004; Kraal et al., 2019). Lepidocrocite is a moderately crystalline Fe(III) mineral that forms in redox-stratified soils and sediments by Fe(II) oxidation and subsequent crystallization of the nucleating Fe(III) particles, usually catalyzed by dissolved Fe(II) (Cornell and Schwertmann, 2003). The surface area (20–100 $m^2\ g^{-1}$; (Poulton et al., 2004)) and PO_4 sorption capacity (100–300 $\mu mol\ g^{-1}$; (Kim et al., 2011; Sleiman et al., 2016)) of Lp are roughly an order of magnitude lower than those of Fh.

Under natural conditions in soils and sediments, FeOx commonly form in the presence of PO_4 (and other strongly-sorbing species) and as a result PO_4 and FeOx can coprecipitate (Schwertmann, 1988). In contrast to PO_4 adsorption onto pre-formed FeOx, which does not impact FeOx structure (Waychunas et al., 1993; Kraal et al., 2019), PO_4 coprecipitation decreases the crystallinity of the resulting Fe(III) precipitate by binding to crystal growth sites. The inhibition of Fe polymerization by PO_4 can lead to very small particles consisting of clusters of Fe polyhedra with large surface area (Rose et al., 1996; Kaegi et al., 2010; Voegelin et al., 2010; Voegelin et al., 2013; van Genuchten et al., 2014b; Senn et al., 2015; van der Grift et al., 2016).

While the impact of PO_4 coprecipitation on FeOx structure is well-studied, the environmental implications remain largely unexplored. Transformation experiments at high temperature and pH (60–70 °C, pH 11–13) have shown that coprecipitation of strongly-sorbing species such as PO_4 and SiO_4 can strongly retard the crystallization of poorly-ordered FeOx (Cornell et al., 1987; Paige et al., 1997). Furthermore, Senn et al. (2017) showed preservation of poorly-ordered, PO_4-bearing FeOx over 30 days at 40 °C and pH 7. These studies invoked decreased FeOx transformation kinetics by PO_4 as it may passivate mineral surfaces and link Fe(III) particles into less reactive aggregates. Conversely, kinetic experiments showed that the dissolution rate of poorly-ordered FeOx exposed to acidic (dilute HCl, pH 2) or reducing (10 $mmol\ L^{-1}$ ascorbic acid) solutions was enhanced by PO_4 coprecipitation (Kraal et al., 2019). Evidently, the effect of PO_4 coprecipitation on FeOx reactivity is ambiguous and, furthermore, only few studies explore PO_4-bearing FeOx transformations under conditions relevant to natural systems.

In natural systems, dissolved Fe(II) and sulfide (denoted here as ΣS(-II), the sum of H_2S, HS^- and S^{2-}) are of particular importance because they are ubiquitous and potent reductants in anoxic sediments. Dissolved Fe(II) adsorbs onto FeOx surfaces and catalyzes crystallization by dissolution-precipitation (Pedersen et al., 2005). Adsorption of dissolved sulfide triggers reductive FeOx dissolution and subsequent precipitation of Fe(II) sulfide when the formed dissolved Fe(II) reacts with additional dissolved sulfide (Dos Santos Afonso and Stumm, 1992). Crystallization and sulfidation diminish the PO_4 retention capacity of Fe (III) precipitates (Krom and Berner, 1980; Senn et al., 2017). For Fe(II)-catalyzed transformation, the effect of PO_4 coprecipitation has so far only been studied on the short timescale (hours) of mineral synthesis (Voegelin et al., 2013; van Genuchten et al., 2014b; van der Grift et al., 2016). Regarding sulfidation, contrasting lines of evidence exist on the impact of PO_4 coprecipitation. It has been suggested that the reaction between FeOx surfaces and dissolved sulfide can be inhibited by PO_4 surface complexes (Biber et al., 1994). Conversely, PO_4 coprecipitation generally decreases the degree of structural order in Fe(III) precipitates, thereby potentially enhancing their reactivity (Kraal et al., 2019).

In a previous set of experiments with natural sediments (Kraal et al., 2020), we explored the impact of PO_4 coprecipitation on Fe(II)-catalyzed crystallization and sulfidation of Fe(III) precipitates formed by Fe(III) hydrolysis and Fe (II) oxidation. While providing insights into the environmental fate of pure and PO_4-bearing FeOx, the highly dynamic field conditions precluded a methodical study of the impact of PO_4 coprecipitation on the transformation of pure and PO_4-bearing FeOx by reaction with dissolved Fe(II) and sulfide. In the current study we aim to provide detailed, mechanistic insight into the impact of PO_4 coprecipitation on environmentally relevant FeOx transformation pathways by exposing pure and PO_4-bearing FeOx to

dissolved Fe(II) and S(-II) under controlled laboratory conditions. We synthesized FeOx with and without coprecipitated PO_4 by Fe(III) hydrolysis and by Fe(II) oxidation at circumneutral pH in the absence or presence of dissolved PO_4. The pure and PO_4-bearing FeOx were suspended in aqueous solutions with dissolved Fe(II) or sulfide at low and high reductant/FeOx ratios (~0.3 and 2 mol mol^{-1}), over time periods of 1–2 weeks. Solution chemistry and FeOx transformations were analyzed using chemical and spectroscopic techniques. Our results show that PO_4 coprecipitation has profound and contrasting effects on Fe(II)-catalyzed transformation and Fe sulfidation. These findings contribute to a better understanding of coupled Fe-P cycling and PO_4 bioavailability in aquatic ecosystems, with particular relevance for eutrophic systems with high dissolved PO_4 concentrations in the sediment that can be resupplied to the water column.

2. MATERIALS AND METHODS

All chemicals used in the experiments were analytical grade or better, except for sodium dithionite (technical grade). All solutions were prepared with ultrapure water (milliQ, 18 MΩ). All glassware was soaked in 1 M HCl and rinsed with milliQ before use.

2.1. Synthesis of the FeOx

Pure Fh and Lp were prepared following established protocols applying base hydrolysis of a concentrated Fe (III) solution and aeration of a concentrated Fe(II) solution, respectively (Schwertmann and Cornell, 1991). In addition, these protocols were adapted to produce Fe(III) precipitates with coprecipitated PO_4, as has been described in detail previously (Kraal et al., 2019; Kraal et al., 2020). In short, PO_4 was added as $Na_2HPO_4 \cdot 4H_2O$ (30–50 mmol L^{-1} PO_4) to the 1 M NaOH solution that was used to establish and maintain the prescribed circumneutral pH during Fe(III) hydrolysis and Fe(II) oxidation. The alkaline PO_4 solution was continuously titrated into the Fe solutions during mineral synthesis over a period of 1–2 hours. The total volume that was added corresponded to a molar P/Fe ratio of 0.1 (10 mol% P relative to Fe) in the system. The Fe precipitates with coprecipitated PO_4 from Fe(III) hydrolysis and Fe(II) oxidation are referred to as P-$FeOx_{HYDR}$ and P-$FeOx_{OXID}$, respectively. After dialysis in milliQ to remove remaining dissolved chemicals, the FeOx were stored as suspensions (~30 mg FeOx L^{-1}) in milliQ in the dark at ~ 4 °C for further experimentation within two weeks after synthesis. Previous work suggested only minor changes to FeOx structure over several weeks under these storage conditions (Kraal et al., 2019).

2.2. Batch FeOx transformation experiments

Anoxic batch reactor experiments were set up to investigate Fe(II)-catalyzed transformation and sulfidation of the four synthetic FeOx. A total of 32 250-mL borosilicate bottles (Schott Duran, Schott AG), with butyl rubber stoppers and polypropylene screw caps with center hole, were used as reactors in which the FeOx were exposed to dissolved Fe(II) or ΣS(-II) at two concentrations (low or high). All bottles were placed in horizontal position on an orbital shaker set at 100 rpm. All treatments were performed in duplicate.

2.2.1. Fe(II)-catalyzed FeOx transformation

Two pH-buffered Fe(II) stock solutions, one with 1.9 and one with 10.7 mmol L^{-1} dissolved Fe(II), were prepared by dissolving appropriate amounts of $Fe(II)SO_4 \cdot 7H_2O$ (Sigma Aldrich) in 2000 mL of anoxic milliQ (grade 5.0 N_2-purged, 60 min). Prior to the addition of $Fe(II)SO_4$, 10 mmol L^{-1} MOPS buffer (Sigma Aldrich) was added and the pH was adjusted to 6.8 with 4 M NaOH. Circumneutral pH 7 is broadly representative for anoxic, Fe(II)-rich freshwater systems and has previously been used in Fe(II)-catalyzed Fe transformation experiments (Hansel et al., 2003; Yang et al., 2010; Han et al., 2020). The headspace of the stock solutions was purged continuously with N_2 during preparation to avoid introduction of O_2. Immediately after adding the $Fe(II)SO_4$, the stock solutions were closed with a butyl rubber stopper and a polypropylene screw cap with center hole, and shaken until the Fe(II) salt was dissolved. Using N_2 overpressure and gas-tight tubing fitted with stainless steel needles, the glass reactor bottles were filled with 200 mL of the appropriate Fe(II) stock solution: eight bottles for low (1.9 mmol L^{-1}) and eight bottles for high (10.8 mmol L^{-1}) Fe(II). Controls were added by filling duplicate bottles with low Fe(II) solution or high Fe(II) solution. Bottles were weighed before and after filling to determine the exact volume of the added Fe(II) solution.

Next, ~ 4 mL of homogenized FeOx suspension was added to each reactor bottle, resulting in an initial FeOx concentration of approximately 7 mmol L^{-1}. The resulting Fe(II)/FeOx-Fe(III) ratio in the bottles was 0.28 for low Fe (II) and 1.6 for high Fe(II). No FeOx suspension was added to the controls. An overview of the (initial) properties of the suspensions is presented in Table 1. At predetermined time steps over a six-day period (T_1–T_4 at 5, 24, 50 and 140 hours), the suspensions were sampled with a plastic 12-mL syringe fitted with a stainless-steel needle. First, a 2-mL sample was taken, immediately filtered over 0.2 µm (nylon syringe filter, M-Filter) into a centrifuge tube containing 200 µL 32% suprapur HCl, resulting in an immediately acidified sample (pH 0). This acidified sample was analyzed for dissolved Fe(II) and PO_4 using the 1,10-phenanthroline and molybdenum blue spectrophotometric assays, respectively (APHA, 2005). Then, an unfiltered 12 mL sample was taken from which two aliquots (1.5 mL and 10.5 mL) were transferred into separate 15-mL centrifuge tubes that were held in liquid N_2 to immediately freeze the suspension and minimize oxidation artifacts. The tubes were subsequently flushed with N_2 and capped. The pre-weighed centrifuge tubes with the 1.5-mL samples were weighed again to verify the volume of suspension in each tube. All samples were stored at − 20 °C until further processing and analysis. The 1.5-mL samples were used for wet chemical sequential Fe extraction (see Section 2.3). Selected 10.5-mL samples were used for Fe

Table 1
Sequential iron and sulfur extraction procedures applied to sub-samples from Fe(II) and ΣH_2S suspensions. Note: except for pH, all values refer to initial values at the start of the FeOx transformation experiments. For FeOx-Fe(III), the standard deviation for the eight bottles per treatment is between parentheses.

Variable	Unit	Low Fe(II)	High Fe(II)	Low ΣS(-II)	High ΣS(-II)
$FeOx\text{-}Fe(III)_{(s)}$	mmol L^{-1}	6.7 (±0.1)	6.6 (±0.1)	6.1 (±0.2)	6.2 (±0.1)
$Fe(II)_{(aq)}$	mmol L^{-1}	1.9	10.7		
Fe(II)/Fe(III)	mol mol^{-1}	0.3	1.6		
Fe(II)/FeOx	mmol g^{-1}	3	17		
$\Sigma H_2S_{(aq)}$	mmol L^{-1}			2.2	9.8
$\Sigma H_2S/Fe(III)_{(s)}$	mol mol^{-1}			0.4	1.6
pH	-	6.8	6.8	8.0	8.0

speciation by synchrotron-based X-ray absorption spectroscopy (XAS; see Section 2.4).

2.2.2. FeOx sulfidation

Two pH-buffered sulfide stock solutions of respectively 2.2 and 9.8 mmol L^{-1} ΣS(-II) were prepared using a concentrated 400 mmol L^{-1} ΣS(-II) master solution prepared with $Na_2S \cdot 9H_2O$ (Sigma Aldrich), verified by iodometric titration (APHA, 2005). The pH of the master solution was set to pH 8.0 in 10 mmol L^{-1} PIPPS buffer (Sigma Aldrich). Total dissolved sulfide, ΣS(-II), consists of approximately 90% HS^- and 10% H_2S at pH 8 in the sulfidation experiment. To prepare the low- and high- ΣS(-II) stock solutions, an appropriate volume of master solution was added to 2000 mL of anoxic milliQ buffered to pH 8.0 with 10 mmol L^{-1} PIPPS buffer. This pH is similar to that of pore-water in anoxic marine sediments with dissolved sulfide (Burdige, 2006). About 200 mL of the appropriate stock solution was transferred to each reaction bottle (eight low ΣS(-II), eight high ΣS(-II)) under N_2 overpressure as described in Section 2.2.1. Duplicate controls of low and high ΣS(-II) were also prepared.

Subsequently, ~ 4 mL of homogenized FeOx suspension was added to each of the 16 bottles with sulfide solution to achieve a concentration of approximately 6 mmol L^{-1} FeOx. The resulting initial ΣS(-II)/FeOx-Fe(III) ratios in the bottles were 0.36 and 1.6 for low and high ΣS(-II), respectively (Table 1). At predetermined time steps over a 14-day period (T_1–T_5 at 0.5, 3.5, 24, 150 and 338 hours), three samples were taken using a plastic 12-mL syringe fitted with a stainless steel needle. First, a 2.5-mL sample was filtered over 0.2 μm, after which sub-samples were immediately used for the measurement of dissolved Fe (II), PO_4 and ΣS(-II) using the phenanthroline, molybdenum-blue and ferric chloride-diamine spectrophotometric assays, respectively (APHA, 2005). Two unfiltered samples were taken for wet chemical sequential extraction of Fe (1 mL in 15-mL centrifuge tube) and S (1 mL in 50-mL centrifuge tube), respectively (see Section 2.3). Finally, an unfiltered 8-mL sample was transferred into a 15-mL centrifuge tube; selected samples were used for synchrotron-based Fe speciation by XAS (Section 2.4). The suspensions for Fe, S and XAS analysis were immediately frozen in liquid N_2, the headspace was flushed with N_2 and the tubes were stored at − 20 °C prior to further processing and analysis.

2.3. Wet chemical sequential extraction of Fe and S pools

The first step of each extraction scheme was applied directly to the frozen aliquots of suspension. To avoid oxidation artifacts, all extraction solutions were deoxygenated with N_2 and the sample tubes were purged with N_2 during chemical change overs between extraction steps. Samples were shaken at 100 rpm during extractions steps, afterwards the samples were centrifuged at 4000 rpm for 20 min and the supernatants were filtered over 0.2 μm. We used two different sequential chemical extraction schemes to separate Fe pools in samples from the Fe(II) and ΣS(-II) suspensions, respectively. For samples from Fe(II) suspensions, we established a sequential Fe extraction scheme that allowed us to distinguish between Fh, Lp and more crystalline phases such as goethite (Gt) and hematite (Ht) (Table 2). Step one (0.5 M HCl, 1 h) was tested using the FeOx synthesized for this study and showed complete dissolution of Fh, P9-$FeOx_{HYDR}$ and P9-$FeOx_{OXID}$ while Lp was mostly preserved (<10% dissolved). Preliminary testing showed that the Lp synthesized for this study (confirmed by X-ray scattering and X-ray absorption measurements) dissolved partially in 1 M HCl (40%) and subsequently in 6 M HCl (60%) (also see SM Section S1). Extraction with hydrochloric acid has the advantage that the oxidation state of Fe is preserved. The analysis of Fe(II) was done using the 1,10-phenanthroline method, after which 0.1 M hydroxylamine-HCl was added to reduce any Fe(III) and total Fe was measured after 24 h. Then, Fe(III) was calculated as the difference between Fe(II) and total Fe.

In order to quantify the temporal evolution of solid-phase Fe(II) and Fe(III) in the samples from the ΣS(-II) suspensions, a series of HCl extraction steps of increasing strength (0.5, 1 and 6 M) was applied to sequentially dissolve Fe phases of increasing crystallinity (Table 2) while preserving Fe oxidation state. The protocol was similar to that of Hellige et al. (2012), who used 0.5 M HCl (1 h) and 6 M HCl (60 °C, 3 days) to determine 'HCl-extractable solid phase-bound Fe(II)' and 'total extractable Fe', respectively, in Lp sulfidation experiments. We note that 6 M HCl at room temperature is commonly intended to extract metastable Fe monosulfide (FeS) but not more crystalline pyrite (FeS_2) (Raiswell and Canfield, 1998; Rickard and Morse, 2005). We note, however, that the results of Hellige et al. (2012) showed that hot 6 M HCl extracted all solid-phase Fe, including minor amounts of

Table 2
Sequential iron and sulfur extraction procedures applied to sub-samples from the Fe(II) and ΣS(-II) suspensions.

Extraction step	Solution	Target iron phases
Fe(II) experiment		
Iron extraction		
Step 1: *0.5 M HCl-Fe*	0.5 M HCl, 1 h	Highly disordered FeOx such as ferrihydrite[1]
Step 2: *hydroxylamine-Fe*	1 M hydroxylammonium-HCl in 25% (v/v) acetic acid	Easily reducible Fe phases such as lepidocrocite[2]
Step 3: *dithionite-Fe*	50 g/L sodium dithionite, 0.35 M acetic acid/0.2 M sodium citrate (pH 4.8)	Crystalline Fe phases such as goethite and hematite[2]
ΣS(-II) experiment		
Iron extraction		
Step 1: *0.5 M HCl-Fe*	0.5 M HCl, 1 h	Highly disordered ferric and ferrous Fe phases such as ferrihydrite and iron monosulfide[1,3]; solid-phase-bound Fe(II)[4]
Step 2: *1 M HCl-Fe*	1 M HCl, 4 h	Reactive Fe phases such as lepidocrocite[5]
Step 3: *6 M HCl-Fe*	6 M HCl, 96 h	Crystalline phases such as goethite and hematite[1,4]
Sulfur extraction		
Step 1: *AVS*	10:2 (v/v) 6 M HCl:1 M ascorbic acid, 16 h	Iron monosulfide[3]
Step 2: S^0	Toluene	Elemental sulfur (S_8^0)[6]

[1]This study; [2]Poulton and Canfield (2005); [3]Rickard and Morse (2005); [4]Hellige et al. (2012); [5]Cornell and Giovanoli (1988) and Claff et al. (2010); [6]Ren et al. (2011).

pyrite (<10% of Fe). As such, the FeS pool reported here may include (minor amounts of) FeS_2 and possibly Fe sulfide intermediates (Wan et al., 2017). This is discussed in more detail in Section 3.3.2 and the Supplementary Material (SM; Section S4.1). Our protocol included an additional 1 M HCl (4 h) step because it has been reported to extract reactive Fe phases such as Lp but not more crystalline phases such as Gt (Cornell and Giovanoli, 1988; Claff et al., 2010). In all extracts, Fe(II) and Fe(III) were measured by 1,10-phenanthroline before and after addition of the reducing agent hydroxylammonium-HCl as described previously. It is important to note that extraction with dilute HCl may introduce artifact Fe(II) in samples containing FeS: H_2S formed during acid dissolution of FeS may react with residual poorly-ordered Fe(III) to form additional, solid phase-bound Fe(II) (Peiffer et al., 2015).

For sequential extraction of reduced inorganic sulfur (RIS) species, we used two steps to dissolve acid-volatile sulfide (AVS) and elemental sulfur (S^0), respectively (Table 2). The method is described in detail elsewhere (Burton et al., 2008; Kraal et al., 2013). Briefly, AVS in the sub-samples was dissolved in 6 M HCl to form H_2S which was precipitated as ZnS in an alkaline Zn acetate trap. The amount of ZnS was measured in a homogenized sub-sample of the trap suspension with the ferric chloride/-diamine spectrophotometric method (Cline, 1969; APHA, 2005). Subsequently, S^0 was extracted with toluene and measured in a filtered aliquot of the toluene supernatant with the cyanide/ferric chloride spectrophotometric method (Bartlett and Skoog, 1954). No additional extraction step for FeS_2 was included because the Fe extraction protocol had already shown full recovery of Fe after 6 M HCl. Again, we note that AVS extracted with 6 M HCl is referred to here as FeS but may include minor amounts of pyrite or iron sulfide intermediates.

2.4. Calculation of dissolved and solid-phase iron and sulfur pools

In the Fe(II)-catalyzed FeOx transformation experiment, 0.5 M HCl-extractable Fe(II) included dissolved Fe(II) and any dissolved Fe(II) that had become associated with the solid phase. In order to use 0.5 M HCl-extractable Fe(II) as a measure of solid-phase-bound Fe(II) (sensu Hellige et al., 2012), it was corrected for dissolved Fe(II) as measured by spectrophotometry in a filtered (0.2 μm) sample aliquot:

$$0.5\,M\ HCl\text{-}Fe(II)_{(s)} = 0.5\,M\ HCl\text{-}Fe(II)_{(tot)} - Fe(II)_{(aq)} \quad (1)$$

During the FeOx sulfidation experiment, < 0.2 μm FeS clusters passed through the filter and interfered with the measurement of 'dissolved' Fe(II) and ΣS(-II). The Fe(II) and ΣS(-II) measurements in the filtrates were corrected for the contribution of < 0.2 μm FeS and these corrected concentrations are presented here. This correction is based on the assumption that when Fe(II) and ΣS(-II) co-occur in the filtrate, 'true' dissolved Fe(II) or ΣS(-II) is the amount of either species that is present in excess over the other with respect to the 1:1 stoichiometry of FeS:

$$Fe(II)_{(aq)} = Fe(II)_{<0.2} - \Sigma S(-II)_{<0.2}\ if\ Fe(II)_{<0.2} > \Sigma S(-II)_{<0.2} \quad (2)$$

$$\Sigma S(-II)_{(aq)} = \Sigma S(-II)_{<0.2} - Fe(II)_{<0.2}\ if\ Fe(II)_{<0.2} < \Sigma S(-II)_{<0.2} \quad (3)$$

The results of the FeS sulfidation experiment also indicated that the measurements underestimated FeS in low-ΣS(-II) suspensions. Therefore, for those samples, FeS was calculated as:

$$FeS = S_{(tot)} - \Sigma S(-II)_{<0.2} - S^0 \quad (4)$$

where total S represents the total amount of S added to the system as ΣS(-II) at the start of the experiment (also see SM, Section S3).

2.5. Iron speciation by spectroscopic analysis

Selected frozen samples were used for Fe speciation by synchrotron-based XAS. Because of time constraints, there was no possibility to measure duplicate samples with XAS and we refer to the duplicate chemical results (Supplementary Material, Tables S2 and S3) to assess reproducibility. The samples were freeze-dried, transferred into an anoxic Ar-purged glovebox and ground with an agate mortar and pestle. Subsequently, an amount of ground sample equal to approximately 1 Fe absorption length (Kelly et al., 2008) was mixed with a small amount of microcrystalline cellulose (Sigma Aldrich) and pressed into a 7 mm-diameter pellet (thickness ~ 1 mm) using a hand-held hydraulic pellet press (Pike Technologies). The pellets were sealed between two layers of Kapton tape. Previous experiments had shown negligible oxidation artefacts for such sealed samples during XAS analysis (Kraal et al., 2019). The sealed samples were packed in Ar-purged gas-tight aluminum laminate bags and transported to the European Synchrotron Radiation Facility (ESRF) in Grenoble (France). Here, Fe K-edge X-ray absorption near-edge spectroscopy (XANES) and extended X-ray absorption fine structure (EXAFS) data were collected at beamline BM26A. Details on the beamline setup can be found in Borsboom et al. (1998) and Nikitenko et al. (2008). At the beamline, sealed samples were placed in the sample holder and spectra were recorded at room temperature in transmission mode from 6962 to 7862 eV, corresponding to a maximum k of 13 $Å^{-1}$ in the EXAFS region. The dimensions of the X-ray beam were 3 × 1 mm (w × h) and the X-ray beam was detuned 30% to prevent second-order harmonics. The XANES region was measured with 0.35 eV steps and step sizes of 0.05 $Å^{-1}$ were used for the EXAFS region. For each sample, at least two spectra were collected and merged, depending on data quality. Data normalization and manipulation were performed using the Athena software package (Ravel and Newville, 2005). The entire EXAFS data set (27 spectra; 22 samples and Fh, Lp, Gt, FeS and aqueous Fe(II)SO_4 reference spectra collected during this and previous synchrotron visits (Kraal et al., 2017; Kraal et al., 2019)) was analyzed with the ITFA software package (Rossberg et al., 2003). Principal components analysis (PCA) was used to determine the number independent components that reproduced the major variance of the entire EXAFS data set (also see SM, Section S4.1). These components were then extracted from the dataset by iterative transformation factor analysis (ITFA), and linear combination fitting (LCF) was used to determine the relative contribution of the independent components to each sample spectrum (i.e. Fe speciation). Considering the practical detection limit of individual mineral classes of 5–10% (O'Day et al., 2004), components with a relative contribution < 5% were omitted from the calculation. The analyses were performed in χ(k) space, using a fitting window of k = 2–11 $Å^{-1}$ of the k^3-weighted EXAFS spectra.

For further characterization of the four FeOx starting materials, subsamples were ground using an agate mortar and pestle and loaded into Kapton capillaries for the collection of high-energy X-ray scattering (HEXS) data suitable for pair distribution function (PDF) analysis. HEXS data were collected at room temperature at beamline 11-ID-B of the Advanced Photon Source (APS) at Argonne National Laboratory (Argonne, Illinois, USA). The X-ray energy during data collection was 58.9 keV and data were collected out to a Q value near 29 $Å^{-1}$. Scattering patterns were corrected for sample-to-detector distance, tilt angle of the detector with respect to the direction of the incident beam, and X-ray polarization and integrated radially using the Fit2D program (Hammersley et al., 1996). The PDFGetX2 program (Farrow et al., 2007) was used to extract the total structure function (S(Q)) and the PDF (G(r)) using standard procedures (Chupas et al., 2003).

3. RESULTS

3.1. Properties of the FeOx starting materials

The structures of the Fe(III) precipitates synthesized for this study, as determined with X-ray absorption spectroscopy (XAS), have been discussed in detail previously (Kraal et al., 2019; Kraal et al., 2020). Complementary X-ray scattering and transmission electron microscopy data that further reveal the FeOx properties are presented in SM Section 4.2. In short, Fe(III) hydrolysis at circumneutral pH in a PO_4-free Fe(III) solution produced pure Fh (Fig. 1, Fig. S8). In the presence of PO_4 (PO_4/Fe = 0.1), Fe(III) hydrolysis formed poorly-ordered FeOx (P-HFO) with a solid-phase P content of 9 mol% (P9-$FeOx_{HYDR}$). Compared to Fh, the Fe K-edge EXAFS spectra for P9-$FeOx_{HYDR}$ showed a less pronounced shoulder feature at k = 5.1 $Å^{-1}$ (Fig. 1A). The second and third peak in the Fourier-transformed (FT) EXAFS spectrum (2.5 and 3.1 Å, uncorrected for phase shift) that represent edge- and corner-sharing octahedra, respectively, were slightly smaller (Fig. 1B). The PDFs show less pronounced peaks for atomic pairs at higher interatomic distance (Fig. 1C). The similarities in the XAS spectra and PDF of Fh and P9-$FeOx_{HYDR}$ indicate that structural differences were minor.

Oxidation of a PO_4-free Fe(II)Cl_2 solution produced pure Lp. The FT EXAFS spectrum (2.6 Å) and PDF (3.0 Å) showed a strongly developed second-shell Fe peak arising from edge-sharing Fe(III) octahedra (Fig. 1, Fig. S8). In the presence of PO_4 (PO_4/Fe = 0.1), a Fe(III) precipitate formed with an overall solid-phase P content

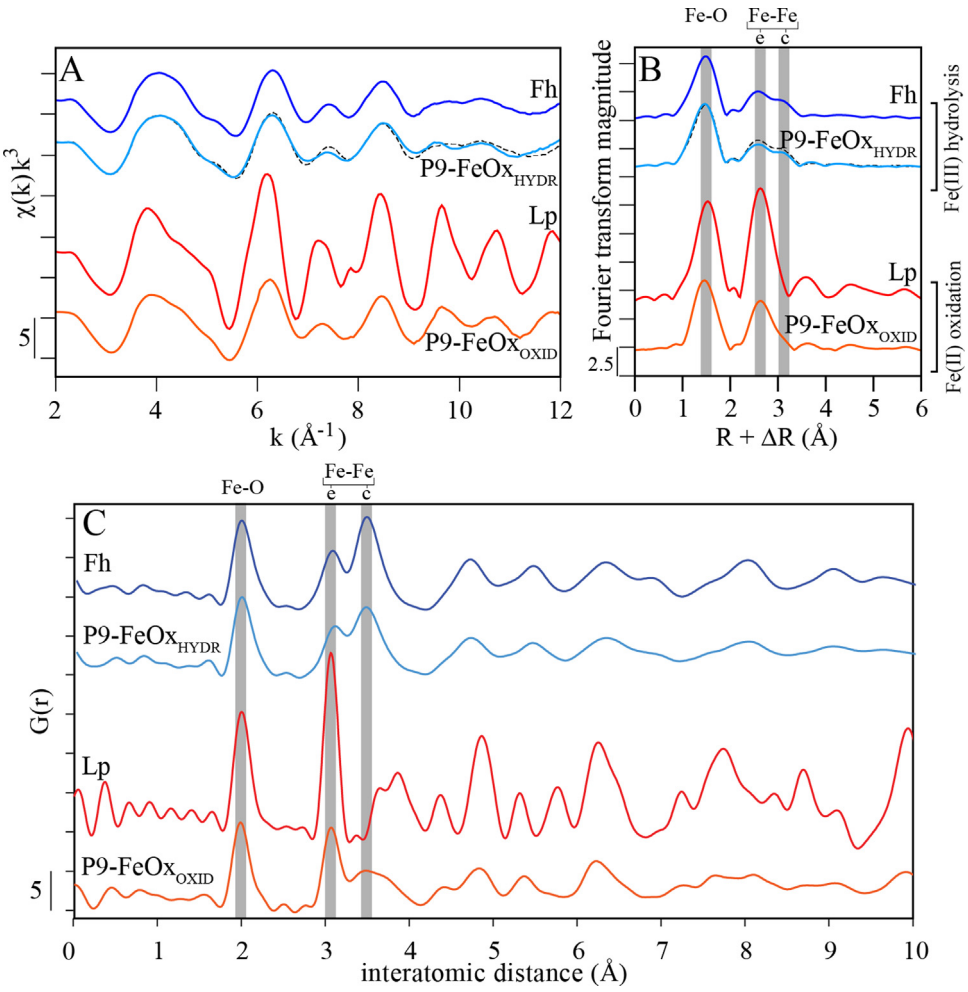

Fig. 1. (A) Fe K-edge EXAFS spectra, (B) Fourier-transformed Fe K-edge EXAFS spectra, and (C) partial pair distribution functions (PDF) of FeOx starting materials. Vertical grey bands in (B) mark magnitude peaks arising from first-shell Fe–O bonds and second-shell edge-sharing (e) and corner-sharing (c) Fe octahedra. The black dashed line plotted with P9-FeOx$_{HYDR}$ shows the Fh spectrum.

of 9 mol% (P9-FeOx$_{HYDR}$). The FT XAS spectrum and PDF for P9-FeOx$_{OXID}$ showed a strong decrease in the magnitude of the edge-sharing Fe-Fe peak together with the emergence of a corner-sharing Fe peak. In addition, the PDF showed strongly suppressed amplitude of peaks between 6.4–9.2 Å, the fingerprint region for Lp including the inter-sheet atomic pair near 8.6 Å (van Genuchten et al., 2014b). The raw high-energy X-ray scattering data for P9-FeOx$_{OXID}$ showed relatively broad, small-amplitude peaks at Q indicative of the presence of Lp. These peaks were superimposed on two broad peaks likely representative of short-range-ordered hydrous ferric oxide (HFO) (Fig. S8). Linear combination fitting using the ITFA-derived components suggests P9-FeOx consists of 30% Lp and 70% HFO (SM, Section S4.2). Indeed, morphologies of Lp and HFO were observed in a P9-FeOx$_{OXID}$ sample analyzed with transmission electron microscopy (TEM) (Fig. S8). These various lines of evidence indicate that P9-FeOx$_{OXID}$ represents a mixture of moderately-crystalline Lp and nanocrystalline HFO.

Besides differences in structure, Lp and P9-FeOx$_{OXID}$ also showed markedly different dissolution kinetics. The less-crystalline P9-FeOx$_{OXID}$ completely dissolved in 0.5 M HCl after 1 h (step 1 of the sequential Fe extraction protocols), which dissolved only 10% of pure Lp.

3.2. Fe(II)-catalyzed FeOx transformation

The dissolved PO_4 concentration was below detection in all Fe(II) suspensions for all timesteps, in the presence of millimolar concentrations of dissolved Fe(II). There was no spectroscopic evidence for precipitation of Fe(II)-PO_4 phases.

3.2.1. Chemical characterization of Fe pools

The dissolved Fe(II) concentration in the low-Fe(II) control was relatively stable at 1.8 ± 0.1 mmol L^{-1} with a maximum value of 1.92 mmol L^{-1} at T_1 and minimum value of 1.72 mmol L^{-1} at T_4 (8% decrease). Dissolved Fe(II) in the high-Fe(II) control was stable throughout the experiment: 10.7 ± 0.2 mmol L^{-1}. After 4 h (T_1), the dissolved Fe(II) in FeOx suspensions had dropped by 0.3 mmol L^{-1} (−15%) and 0.7 mmol L^{-1} (−7%) compared to initial concentrations in low-Fe(II) and high-Fe(II) suspensions,

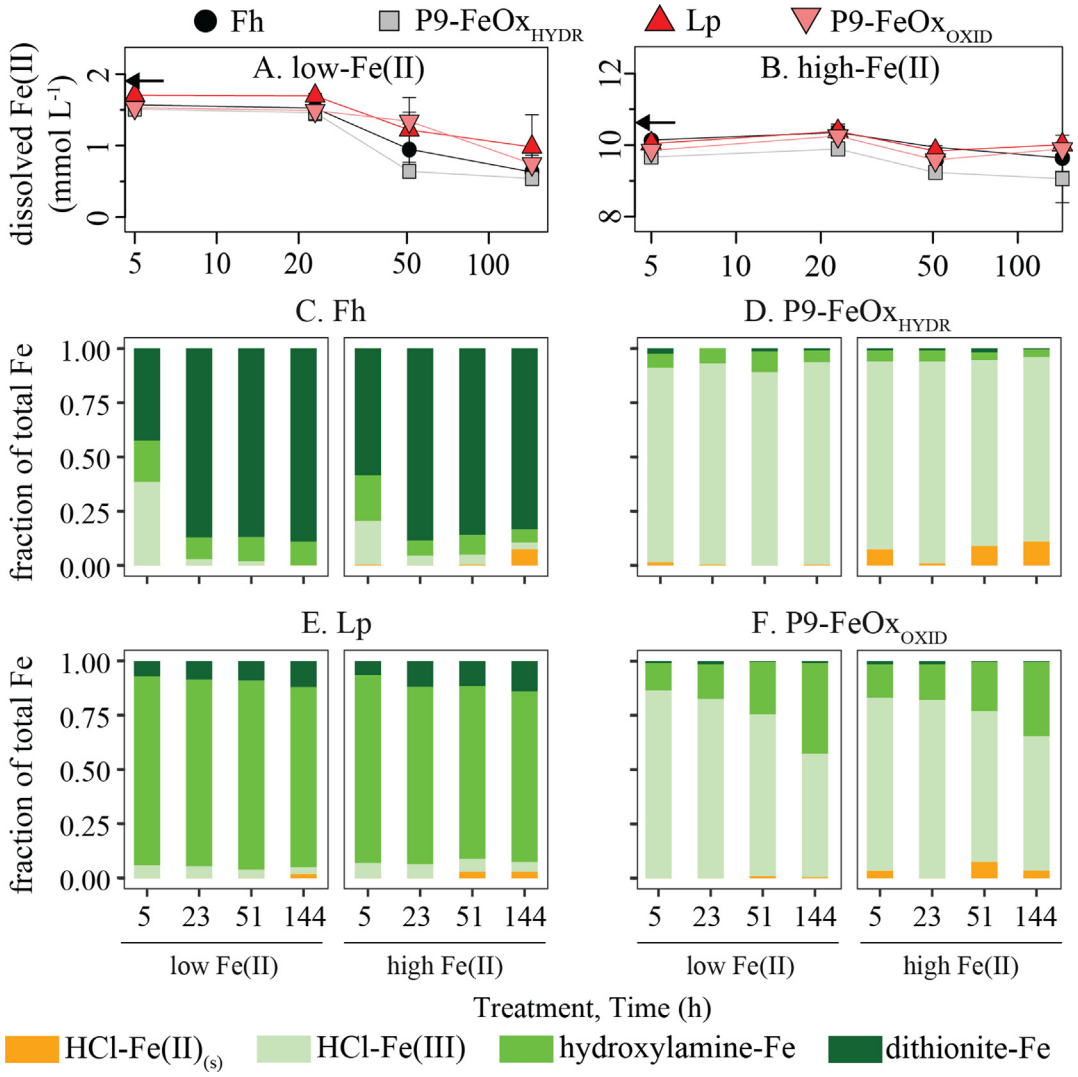

Fig. 2. Dissolved Fe(II) concentrations (A, B) and chemical sequential iron extraction results (C–F), plotted against time. 0.5 M HCl-Fe(II)$_{(s)}$ refers to solid-phase-bound Fe(II), calculated as the difference between 0.5 M HCl-Fe(II) and dissolved Fe(II) (Eq. (1)). Error bars in dissolved Fe(II) plots represent standard deviation (n = 2). Black arrows indicate the Fe(II) concentrations at T_1 (5 h) in controls without FeOx. Time is plotted on a logarithmic x axis in panels A and B.

respectively (Fig. 2A, B). The dissolved Fe(II) concentrations in low-Fe(II) suspensions then remained stable up to 24 h (1.6 ± 0.1 mmol L^{-1}, $n = 16$), followed by a decrease to eventually 0.7 ± 0.2 mmol L^{-1}. The overall decrease in dissolved Fe(II) of 1.2 mmol L^{-1} represented ~ 60% of initial dissolved Fe(II) for low-Fe(II) suspensions. Assuming that the cause was Fe(II) precipitation, this represents 10–15% of total solid-phase Fe, i.e. initial FeOx-Fe(III) plus precipitated Fe(II). In the high-Fe(II) suspensions, between 4 and 144 h, the dissolved Fe(II) concentration was generally stable in all suspensions (9.9 ± 0.4 mmol L^{-1}, $n = 32$). About 10% of dissolved Fe(II) became associated with the solid-phase Fe during the high-Fe(II) experiment, which similar to low-Fe(II) would represent 10–15% of total solid-phase Fe.

On average, for all samples ($n = 64$), the chemical sequential Fe extraction recovered 101 ± 10% of total Fe, i.e. the sum of initially added FeOx-Fe(III) and dissolved Fe(II). In Fig. 2, we report only solid-phase Fe as determined by sequential chemical extraction and omit dissolved Fe(II): solid-phase 0.5 HCl-Fe(II)$_{(s)}$ was calculated as the difference between 0.5 M HCl-Fe(II) and dissolved Fe(II) (Eq. (1)). Poorly-ordered Fh underwent complete transformation from labile Fe(III) to easily-reducible and crystalline Fe, with more rapid transformation under high Fe (II) (Fig. 2C). By contrast, only 10% of P9-FeOx$_{HYDR}$ transformed to easily-reducible Fe while no crystalline Fe formed (Fig. 2D). Limited transformation was also observed for Lp, of which a small part (10–15%) transformed from easily-reducible to crystalline Fe (Fig. 2E). The PO_4-bearing Fe(II) oxidation product P9-FeOx$_{OXID}$ showed more extensive transformation: gradually, 35–45% of poorly-ordered Fe(III) was transformed into easily-reducible Fe(III) (Fig. 2F). For all FeOx, the extent of

transformation at the end of the experiment was similar under low and high Fe(II).

Despite a 60% decrease in dissolved Fe(II) in low-Fe (II) suspensions, no 0.5 M HCl-Fe(II)$_{(s)}$ was observed except for a small fraction in the Lp suspension (<5%). It is possible that formerly dissolved Fe(II) became associated with more crystalline phases and was therefore extracted during step 2 or 3 of the protocol. We also note that 0.5 M HCl-Fe(II)$_{(s)}$ is a calculated variable (Eq. (1)) that represents a small fraction of total solid-phase Fe (10–15%) and is therefore difficult to quantify reliably. In high-Fe(II) suspensions, the sequential chemical Fe extraction indicated that small amounts of 0.5 M HCl-Fe(II)$_{(s)}$ were present (5–15% of total solid-phase Fe), similar to expected values based on Fe aforementioned budget calculations (10–15%).

3.2.2. Comparison of chemical and spectroscopic Fe characterization

From the chemical extractions, it was apparent that differences in Fe transformation between low- and high-Fe(II) suspensions were limited. To optimize our use of limited beamtime, we focused on analyzing samples from the start and end of the low-Fe(II) incubation experiment. Data analysis by iterative transformation factor analysis (ITFA) indicated that the sample spectra could be reproduced as linear combinations of four independent components that represent Fh, Lp, Gt and a ferrous Fe(II) species. Ferrous Fe likely represents a mixture of adsorbed and dissolved Fe (II), the latter precipitated as Fe(II) salt during freeze-drying of the suspension prior to XAS analysis (also see SM Section S4.1). As expected, the ITFA-LCF component FeS was not detected in the Fe(II) suspensions in the absence of ΣS(-II). There was good agreement between Fe pools as determined by chemical dissolution and XAS, with regression R^2 for individual Fe pools (0.5 M HCl-Fe(III)–HFO; hydroxylamine–Lp; dithionite–Gt) between 0.88 and 0.92. This indicated that 0.5 M HCl-Fe(III) reliably represented the poorly-ordered starting materials Fh and P9-FeOx$_{HYDR}$, as well as the mixed-phase P9-FeOx$_{OXID}$. For the latter, this reflected the poorly-crystalline and thus labile nature of its Lp component. Furthermore, hydroxylamine-Fe and dithionite-Fe were useful as measures for Lp and Gt, respectively. Some notable differences between chemical and spectroscopic results were also observed. Firstly, the extent of Fh crystallization as determined by XAS (~70%) was relatively low compared to chemical results (100%) (Fig. 3A). Secondly, the chemical results for P9-FeOx$_{OXID}$ showed a gradual increase in the amount of easily-reducible Fe at the expense of labile Fe(III) over the course of the experiment (Fig. 2F). By contrast, the XAS results indicated an increase of the Lp component from 30 to 50% in the first four hours, after which it remained stable. Thirdly, the ITFA-LCF results for low Fe(II) indicated that 5–10% of total Fe was present as (aqueous or poorly-ordered) Fe(II), which was lower than the chemical results (10–20%) and lower than the calculated Fe(II) contribution of 20% to total Fe ($Fe(II)_{tot}/Fe_{tot} = 0.2$).

3.3. Reaction of FeOx with dissolved ΣS(-II)

3.3.1. Dissolved Fe(II), PO_4 and ΣS(-II)

Low- and high- ΣS(-II) controls showed a loss of 5–15% of sulfide over two weeks. The initial concentrations of ΣS(-II) in the reaction bottles before FeOx addition were 2.2 ± 0.1 and 9.8 ± 0.8 mmol L^{-1} for low and high ΣS(-II), respectively. In low-ΣS(-II) suspensions, dissolved Fe (II) and ΣS(-II) concentrations were below 10 and 30 μmol L^{-1}, respectively, throughout the sulfidation experiment (Fig. 4). These concentrations represented negligible amounts (<2%) of initial FeOx-Fe (6.5 mmol L^{-1}) and ΣS(-II) (2.2 mmol L^{-1}), respectively. Concentrations of PO_4 reached 45 and 140 μmol L^{-1} in the suspensions with P9-FeOx$_{HYDR}$ and P9-FeOx$_{OXID}$, respectively, representing approximately 10% and 20% of total initially coprecipitated PO_4 (Fig. 5F, L).

In high-ΣS(-II) suspensions, the dissolved ΣS(-II) concentration showed a continuous decrease (P9-FeOx$_{HYDR}$ > Fh = P9-FeOx$_{OXID}$ > Lp), becoming depleted by T_5 (344 h) in all suspensions except Lp (Fig. 5A, D, G, J). Dissolved Fe(II) concentrations were consistently near-zero for Fh and Lp, while PO_4-bearing FeOx showed accumulation of dissolved Fe(II) – meaning Fe(II) < 0.2 μm – in later stages of the FeOx sulfidation experiment, co-occurring with ΣS(-II) depletion (Fig. 5B, E, H, K). The dissolved Fe(II) concentrations at 344 h represented up to 20% and 10% of total Fe in suspensions with P9-FeOx$_{HYDR}$ and P9-FeOx$_{OXID}$, respectively. The fraction of PO_4 released into solution during transformation of the PO_4-bearing FeOx was high from 5 h onwards (60%) and showed similar increases over time for P9-FeOx$_{HYDR}$ and P9-FeOx$_{OXID}$, up to 75% of total P at 344 h (Fig. 5F, L).

3.3.2. Chemical characterization of Fe and S pools

In low-ΣS(-II) suspensions, the total fraction of Fe(III) that was reduced to Fe(II) – the sum of Fe(II) sequentially extracted in 0.5 M, 1 M and 6 M HCl – was similar for all FeOx throughout the experiment (0.29 ± 0.05, $n = 40$). The Fe(II) pool consisted predominantly of non-sulfidized Fe (II) and about 5% of Fe(II) was present as sulfidized Fe (FeS) (Fig. 5A–D). For the Lp starting material, the FeS fraction was slightly higher (0.06 ± 0.02) than for the other FeOx (0.03 ± 0.01) (Fig. 5C). For Fh, P9-FeOx$_{HYDR}$ and P9-FeOx$_{OXID}$, all Fe(III) was present as 0.5 M HCl-Fe (III). In Lp suspensions, the proportion of crystalline Fe (III), i.e. 6 M HCl-Fe(III), increased from 55 to 70% of total Fe(III), compared to 60% for the Lp starting material (see SM, Section S1). Dissolved ΣS(-II) was depleted from 5 h onwards and S was predominantly present as S^0 (80–90% of total S) complemented by a relatively small pool of FeS (Fig. 6).

In high-ΣS(-II) suspensions with Fh, P9-FeOx$_{HYDR}$ and P9-FeOx$_{OXID}$, 30–60% of FeOx-Fe(III) was already sulfidized after 5 h, increasing to 85–95% sulfidation at 344 h (Fig. 5A, B, D). The P9-FeOx$_{HYDR}$ suspension showed most rapid (T_1) and extensive (T_5) sulfidation. Non-sulfidized Fe(II) was an extraction artifact (see Section 2.3) and therefore treated as Fe(III) (hatched

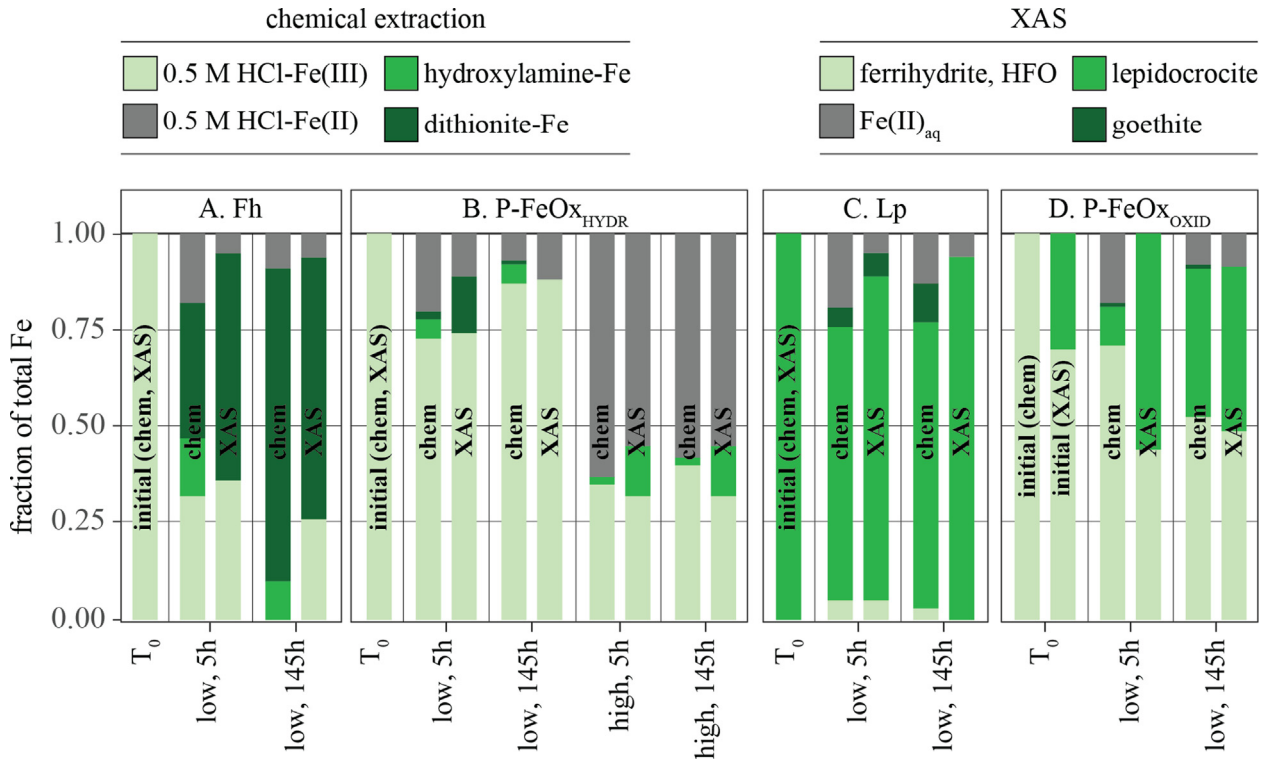

Fig. 3. Comparison of results from chemical sequential iron extraction (chem) and Fe K-edge EXAFS (XAS) for Fe species in FeOx starting materials (T_0) and in selected samples from T_1 (5 h) and T_4 (145 h). Note that 0.5 M HCl-Fe(II) includes dissolved and solid-phase-bound Fe (II). Legend indicates Fe pools based on chemical extraction (left) and XAS (right).

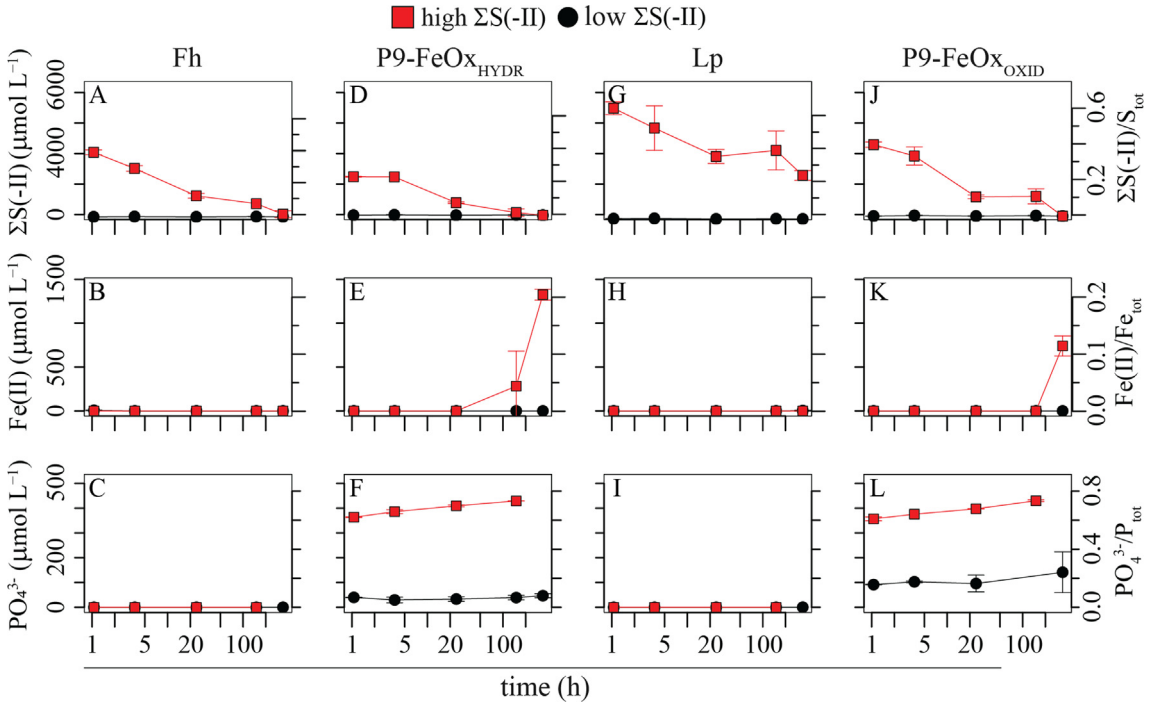

Fig. 4. Concentrations of dissolved ΣS(-II), Fe(II) and PO_4 plotted against time in suspensions of the four FeOx under low- ΣS(-II) (2 mmol L^{-1}) and high-ΣS(-II) (10 mmol L^{-1}) suspensions. The dissolved Fe(II) and ΣS(-II) concentrations were corrected for FeS nanoclusters as described in the SM, Section S2. For each plot, left y axis shows concentration and right y axis show the solute as fraction of total S, Fe or P in the system. Note the logarithmic x axis (time).

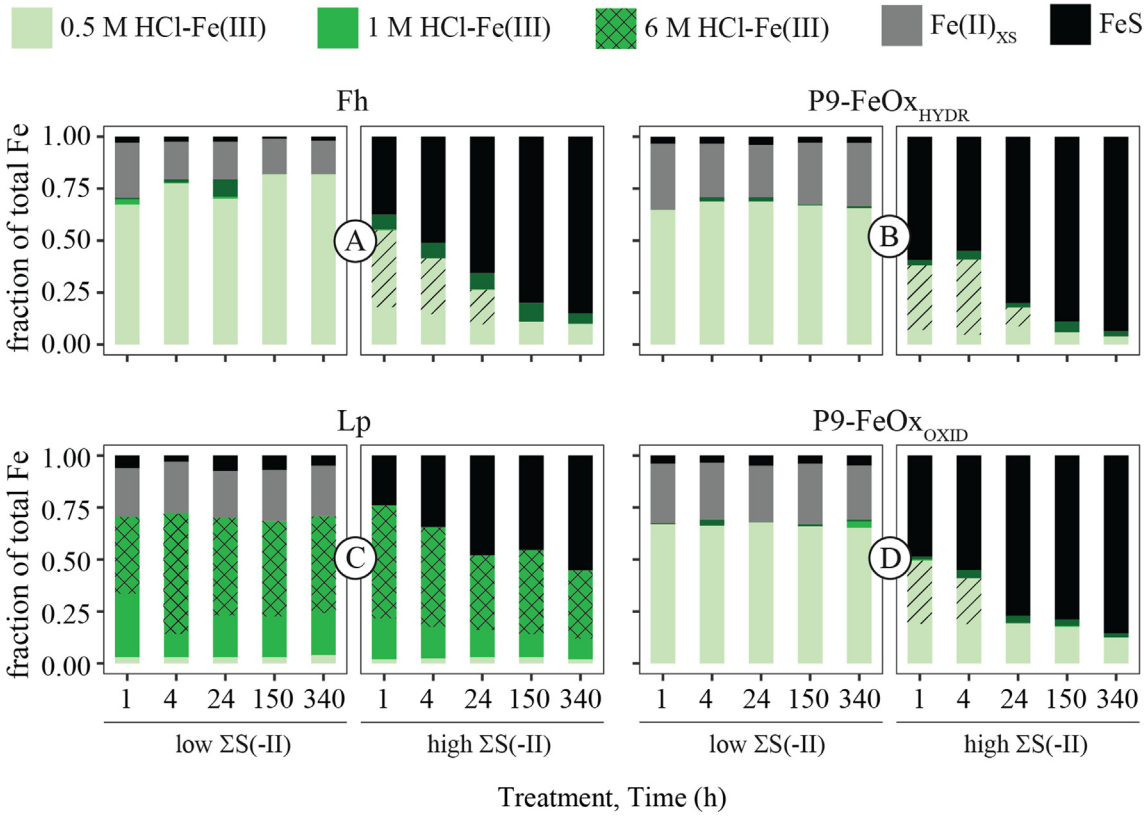

Fig. 5. Chemical sequential Fe extraction results plotted against time for the four different FeOx (A–D) under low (2 mmol L^{-1}) or high (10 mmol L^{-1}) initial dissolved HS^-. $Fe(II)_{XS}$ is excess, non-sulfidized ferrous Fe. Striped areas in 0.5 M HCl-Fe(III) indicate the part that was reduced during extraction (see Section 2.3 for details). Data also in SM, Table S3.

light-green areas in Fig. 5). The sequential S extraction showed that S^0 as fraction of total S was similar in Fh, P9-$FeOx_{HYDR}$ and P9-$FeOx_{OXID}$ suspensions and remained relatively constant over the course of the experiment (0.37 ± 0.05, $n = 30$). The increase in FeS over time for Fh, P9-$FeOx_{HYDR}$ and P9-$FeOx_{OXID}$ was mirrored by a decrease in dissolved ΣS(-II) (Fig. 6A, B, D). In Lp suspensions, the fraction of sulfidized Fe under high ΣS(-II) was low (0.2 to 0.5 between T_1 and T_5, Fig. 5C), relatively high concentrations of dissolved ΣS(-II) persisted (2 mmol L^{-1} after 344 h, Fig. 4G) and the S^0 pool as fraction of total S was small (0.26 ± 0.04, $n = 10$) (Fig. 6C). Furthermore, FeS accounted for all Fe(II) in the samples and no artifact Fe(II) was detected. The 1 M HCl-Fe(III):6 M HCl-Fe(III) ratio in the Lp suspensions was 0.35 ($n = 10$), which was low compared to the Lp starting material (0.65).

3.3.3. Comparison of chemical and spectroscopic Fe characterization

The ITFA-LCF results indicated that the Fe sulfide phase consisted of iron monosulfide (FeS). There was no evidence for a significant (>5–10% of Fe) pool of pyrite (FeS_2), which has a distinct Fe K-edge EXAFS spectrum that was not observed in any of the samples from the sulfidation experiment (see also SM, Section S4.1). The chemical and spectroscopic results showed similar extents of FeOx sulfidation (R^2 for FeS = 0.92), with a relatively large difference for Lp, 40 versus 25% of total Fe (Fig. 7C). The EXAFS analysis indicated limited crystallization of the initial FeOx: only small fractions of the poorly-ordered FeOx (Fh, P9-$FeOx_{HYDR}$ and P9-$FeOx_{OXID}$) were transformed into Lp or Gt, and similarly the Lp starting material showed nearly no transformation into more crystalline Fe (III) (Gt) during the experiment. The EXAFS results indicated relatively small pools of non-sulfidized Fe(II), only in the samples from low-ΣS(-II) suspensions. This contrasts with chemical results that showed large pools of non-sulfidized Fe(II) in samples under high ΣS(-II), further supporting the notion that this Fe(II) was an artefact of chemical Fe extraction.

4. DISCUSSION

4.1. Structural alteration of Fe(III) precipitates by PO_4 coprecipitation

The impact of PO_4 coprecipitation on the short-range structure of the FeOx starting materials used in this study has been discussed in detail elsewhere (Kraal et al., 2019; Kraal et al., 2020). Here, we discuss key aspects of the Fe (III) precipitates used in this study.

Sorption of PO_4 onto freshly-formed Fe(III) oligomers and polymers, i.e. coprecipitation, inhibits further Fe(III) polymerization and crystallization, resulting in decreased

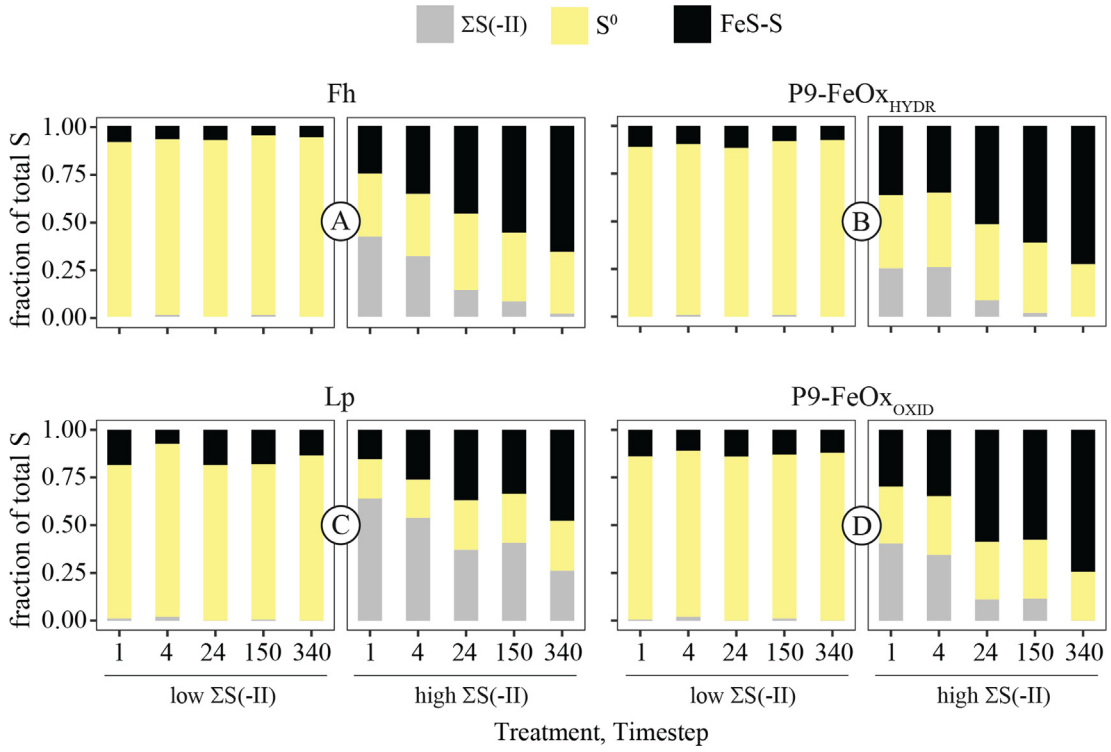

Fig. 6. Time evolution of chemical S fractionation for the four FeOx (A–D) under low (2.2 mmol L^{-1}) and high (9.8 mmol L^{-1}) initial dissolved ΣS(-II). Data also in SM, Table S3.

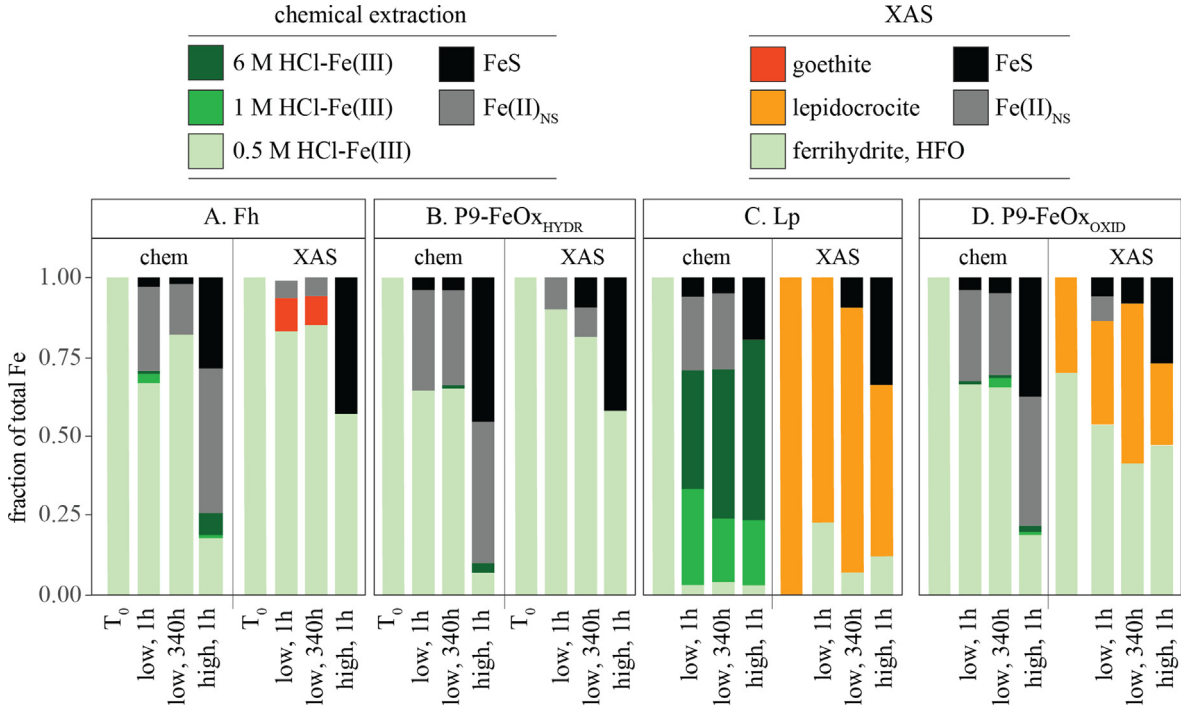

Fig. 7. Comparison of Fe speciation by chemical extraction and Fe K-edge EXAFS for selected samples from the low- and high-ΣS(-II) (l) Fe(III) sulfidation experiment.

short-range structural order of Fe(III) precipitates (Rose et al., 1996; Voegelin et al., 2010; van Genuchten et al., 2014b). The extent of the impact depends on FeOx formation pathway and relative PO_4 abundance. Rapid base hydrolysis of Fe(III) produces poorly-ordered FeOx even in pure Fe(III) solution and coprecipitation of PO_4 at P/Fe = 0.1 mol mol^{-1} led to only a minor decrease in structural order (Fh versus P9-FeOx$_{HYDR}$; Fig. 1). With increasing P/Fe, Fe(III) hydrolysis will shift to formation of Fe-PO_4 colloids rather than PO_4-bearing FeOx (Rose et al., 1996). The coprecipitation of oxyanions such as PO_4, SiO_4 and AsO_4 during Fe(III) hydrolysis may increase surface area and reactivity of Fe(III) precipitates (Waychunas et al., 1993; Pokrovski et al., 2003; Kraal et al., 2019).

Coprecipitation of PO_4 during Fe(II) oxidation has been used to synthesize PO_4-bearing Fe(III) precipitates in various studies (e.g. Kaegi et al., 2010; Voegelin et al., 2010; Voegelin et al., 2013; van Genuchten et al., 2014a; Senn et al., 2015; van der Grift et al., 2016). In these studies, Fe(III) precipitation was initiated in an originally PO_4-rich solution, which resulted in sequential formation of Fe(III)-P, P-rich HFO and Lp as PO_4 was rapidly depleted by sorption onto nucleating Fe(III) particles. In our study, even though PO_4 was added continuously, Fe (III) phases of varying structure were also observed, suggesting that Fe precipitation follows competing pathways and lepidocrocite formation is kinetically not fully suppressed even when PO_4 is constantly provided. The poorly ordered and labile nature of the Lp phase in P9-FeOx$_{OXID}$ was reflected in both the X-ray characterization data (absence of sheet-stacking Fe-Fe atomic pairs) and chemical result (solubility in 0.5 M HCl, which dissolves poorly-ordered Fe(III) phases but not pure Lp).

4.2. Fe(II)-catalyzed transformation of Fh and Lp

In the presence of dissolved Fe(II), pure Fh rapidly transformed to Gt (90%) and minor amounts of Lp (10%), the rate positively correlated to the Fe(II) concentration (Fig. 4). Based on negligible structural Fh transformation in Fe(II)-free solution over up to four weeks reported previously (Kraal et al., 2019), we attribute the Fh transformation to Fe(II)-catalyzed crystallization. No magnetite (Mag) was observed, despite high Fe(II) concentrations and high Fe(II)/FeOx ratios (Table 1) that can favor rapid Mag formation during Fe(II)-catalyzed Fh transformation (Tronc et al., 1992; Hansel et al., 2005; Yang et al., 2010). Although not detected in the XAS data, Mag may have been extracted by dithionite (Claff et al., 2010) in the chemical Fe analysis and thus misconstrued as crystalline Fe(III) (Table 2). From the decrease in dissolved Fe(II) and the Fe (II)/Fe$_{tot}$ ratio in Mag (0.3: Fe(II)Fe(III)$_2$O$_4$), we can estimate the potential Mag fraction. In low-Fe(II) suspensions, removal of $\sim$ 1 mmol L^{-1} of dissolved Fe(II) could have formed $\sim$ 3 mmol L^{-1} Mag, which would represent about 40% of total Fe in the system (8.6 mmol Fe L^{-1}). However, there was no indication for Mag in the spectroscopic data (Fig. 4). Furthermore, the distinct black color of Mag, which would have been apparent if Mag occurred as significant Fe pool (Hansel et al., 2003), was not observed in low- or high-Fe(II) suspensions (see SM, Section S5). The lack of Mag formation in our experiments may be due to rapid destabilization of the Fh crystal lattice upon Fe(II) adsorption (Manceau and Drits, 1993; Pedersen et al., 2005), which favors Lp and Gt formation by dissolution-precipitation over solid-state Mag formation (Tronc et al., 1992; Yang et al., 2010). Furthermore, the relatively low pH (6.8) in the Fe(II)-FeOx suspensions may have inhibited Mag formation (Hansel et al., 2003). The chemical results showed that part of the solid-phase Fe (II) was retrieved as surface-bound Fe(II) (Fig. 4), the remainder may have been incorporated into more crystalline phases, potentially by electron transfer from surface-bound Fe(II) into FeOx particles.

The other pure FeOx starting material used in this study, Lp, underwent minor transformation into Gt (5–10%) over the course of the six-day experiment, irrespective of Fe(II) concentration (Fig. 4). Previously, Yan et al. (2015) found microscopic (unquantified) evidence for transformation of Lp to Gt via dissolution-precipitation at molar Fe(II)/FeOx-Fe(III) above 0.02 (our study: 0.3 and 1.6 for low and high Fe(II), respectively; Table 1). With dissolution as a prerequisite for transformation to Gt (Schwertmann and Taylor, 1972; Cudennec and Lecerf, 2005), lower Fe (II)-induced solubility of Lp compared to Fh can explain the limited extent of transformation of the former. In line with this, Senn et al. (2017) found only a slight increase in crystallinity of Lp over a 30-day aging experiment conducted at pH 7 and 40 °C. Conversely, extensive Lp crystallization to Gt was observed within hours under more extreme conditions of high pH (12) and temperature (70–80 °C) (Schwertmann and Taylor, 1972). Overall, our results for Fh and Lp show strongly contrasting susceptibility to Fe(II)-catalyzed transformation, while indicating that dissolved Fe(II) concentration does not exert significant control over the extent of transformation.

4.3. PO_4 coprecipitation alters reactivity of FeOx towards Fe (II)

The impact of PO_4 coprecipitation on Fe(II)-catalyzed transformation differed with FeOx synthesis pathway. For Fe(III) hydrolysis – producing Fh and P-HFO, PO_4 coprecipitation resulted in minor alteration of short-range structure but strongly suppressed Fe(III) crystallization. Previous studies with poorly-ordered FeOx from Fe(III) hydrolysis also found that coprecipitation of strongly-sorbing oxyanions such as PO_4 and SiO_4 at oxyanion/Fe ratios as low as 0.03 (our study: 0.1) strongly retarded Fe (III) crystallization under high T (60–70 °C) and pH (11–13), strongly favorable to transformation (Cornell et al., 1987; Paige et al., 1997).

This reduced reactivity can be attributed to FeOx surface passivation by PO_4 surface complexes (Majzlan, 2011). Most coprecipitated PO_4 was likely present on the surface of P9-FeOx$_{HYDR}$: Fh has a large surface-to-bulk ratio (Hiemstra, 2013) and PO_4 sorbs as terminal (surface) groups on Fe(III) polymers (Rose et al., 1996). Under the experimental conditions, Fe(II) may have sorbed onto surface PO_4 complexes rather than the Fh surface: modelling

indicates that at pH 6.8, PO_4 surface complexes exist predominantly as bidentate $Fe_2O_2PO_2$ geometries with negative charge on the phosphate group (Antelo et al., 2010), while the point-of-zero charge of Fh is ~ 8 (Hiemstra and Van Riemsdijk, 2009; Antelo et al., 2010) and thus the mineral surface would have been positively charged. Similar abundances of coprecipitated PO_4 (P/Fe = 0.1) and sorbed Fe(II) ($Fe(II)_{tot}$/FeOx-$Fe(III)_{tot}$ = 0.05–0.1) suggest that Fe (II) binding onto PO_4 surface complexes could have efficiently shielded the Fh surface from direct contact with Fe(II) and subsequent transformation initiated by electron transfer (Sherman, 1987; Pedersen et al., 2005).

In the case of Fe(II) oxidation, by contrast, PO_4 coprecipitation shifted the reaction product from moderately crystalline and stable Lp to a mixture of P-HFO and poorly-crystalline Lp (P9-$FeOx_{OXID}$) that was more susceptible to Fe(II)-catalyzed crystallization. The combined chemical and spectroscopic results indicate that crystallization entailed transformation of poorly-ordered P-HFO and moderately-crystalline Lp into more crystalline Lp, without further transformation into crystalline phases such as Gt. It seems that coprecipitation of PO_4 during Fe(II) oxidation can be an efficient PO_4 sink, but the resulting labile PO_4-bearing FeOx may be relatively susceptible to crystallization mechanisms that eventually diminish the PO_4 retention capacity of Fe minerals (Senn et al., 2017). Actual release of PO_4 during FeOx crystallization was not observed. This can possibly be attributed to the presence of dissolved Fe^{2+}, which may have precipitated dissolved PO_4 to form vivianite in minor amounts that remained undetected. Furthermore, PO_4 may have been adsorbed onto remaining FeOx surfaces.

In summary, coprecipitation of PO_4 at relatively low and naturally relevant P/Fe (0.1) favors the formation and preservation of poorly-ordered FeOx with high PO_4 retention capacity. The persistence of such FeOx depends in part on the formation pathway, i.e. Fe(III) hydrolysis versus Fe(II) oxidation. Crystallization diminishes the sorption capacity of FeOx and leads to release of PO_4 (Senn et al., 2017; Senn et al., 2018), and therefore the PO_4-induced persistence of poorly-ordered FeOx may affect the nutrient and contaminant retention capacity of natural sediments on short timescales relevant to dynamic natural systems.

4.4. Reduction and sulfidation of pure and PO_4-bearing FeOx

The capacity of the FeOx to scavenge sulfide was compared based on dissolved sulfide consumption after 1 h (T_0–T_1): P9-$FeOx_{HYDR}$ > P9-$FeOx_{OXID}$ > Fh > Lp (Fig. 4). This contrasts with the large difference (order of magnitude) in reactivity of Fh ≫ Lp towards sulfide on very short timescales of seconds to minutes (Poulton et al., 2004) and suggests that Fh and Lp consume sulfide at more similar rates on longer timescales that are relevant to biogeochemical processes in natural sediments.

After adsorption of sulfide to the FeOx surface, electrons are transferred from S(-II) to Fe(III), resulting in formation of elemental sulfur (S^0) and reduced Fe(II) at the mineral surface. The subsequent reactions depend on the electronic properties of the FeOx and the relative abundances of Fe and ΣS(-II). In the presence of excess ΣS(-II), the Fe(II) can then react to form Fe(II)S either at the mineral surface or in solution after detachment from the bulk mineral (Dos Santos Afonso and Stumm, 1992; Poulton et al., 2004; Hellige et al., 2012; Peiffer et al., 2015). When ΣS(-II) is low relative to FeOx-Fe(III), sulfide is rapidly depleted and the reaction products are S^0 and non-sulfidized, surface-associated Fe(II) (Peiffer et al., 2015). Over time, pyrite can form at the mineral surface, likely with a key role for polysulfides formed by reaction of S^0 with aqueous ΣS(-II) (Rickard, 1975; Wan et al., 2017). In previous sulfidation experiments under similar Fe(III)/ΣS(-II), only minor (≤10% of total Fe) amounts of pyrite formed over two weeks and only in case of excess Fe(III) similar to our low-ΣS(-II) treatment (ΣS(-II)/Fe(III) = 0.4).

The variable reaction pathways as a function of the relative abundance of ΣS(-II) are reflected in our results. In low-ΣS(-II) suspensions (initial ΣS(-II)/Fe(III) = 0.4), the abundance of reactive surface sites led to rapid depletion of ΣS(-II) by oxidation to S^0 with concurrent reduction of Fe(III) to non-sulfidized Fe(II). The combined chemical and spectroscopic results may shed some light on the nature of the non-sulfidized Fe(II) pool. The spectroscopic data indicated a non-sulfidized Fe(II) pool (<10% of total Fe) that was significantly smaller than bulk Fe(II) as determined by chemical extraction (20–30%) (Fig. 7). The component representing non-sulfidized Fe(II) extracted from the EXAFS dataset by ITFA was similar to aqueous Fe (II) and could represent surface-bound Fe(II). The remainder (70–90%) of the non-sulfidized Fe(II) identified with sequential extraction was likely present as bulk Fe(II), formed by electron transport from surface-associated Fe (II) into the bulk mineral. Assuming that this structural Fe(II) does not alter the Fe binding environment in Fh and Lp significantly, it is likely to escape detection by spectroscopic means such as XAS or Mössbauer (Hellige et al., 2012; Peiffer et al., 2015; Peiffer and Wan, 2016). Furthermore, rapid surface-to-bulk electron transport would regenerate surface Fe(III) and inhibit detachment of Fe(II) from the mineral surface, which may explain the lack of dissolved Fe(II) accumulation in low-ΣS(-II) suspensions (Fig. 4).

In all low-ΣS(-II) suspensions, sulfide was rapidly oxidized by reaction with excess Fe(III) and therefore, no major differences in the extent of Fe reduction or sulfidation were observed between pure and PO_4-bearing species (Fig. 6). Furthermore, there were only minor changes in Fe speciation between 1 h and 14 days (T_1–T_5). By contrast, previous work (Peiffer et al., 2015) showed complete transformation of 6-line Fh into more crystalline phases such as pyrite (FeS_2, 30% of total Fe) and Gt, Ht and Mag over two weeks at similar pH (7) and under a similar initial molar ΣS (-II)/ Fe(III) (0.6) as used in this study (0.4). Perhaps this discrepancy highlights the large impact that (small) initial differences in FeOx structure can have on short-term reductive transformation of FeOx.

Under high ΣS(-II) (initial ΣS(-II)/Fe(III) = 1.7), chemical extraction showed large pools of sulfidized Fe. The combined chemical and spectroscopic results indicate that

sulfidized Fe was predominantly FeS. Pyrite may have occurred in minor amounts (<5% of Fe) that escaped detection by XAS (O'Day et al., 2004), even though it is unlikely to form on short timescales under excess S(-II) (Wan et al., 2017). Non-sulfidized Fe(II) was disregarded as an extraction artifact, also supported by the XAS data from high-ΣS(-II) samples that did not show Fe(II) phases other than FeS (Fig. 7). The extent of initial (0–1 h) FeOx sulfidation mirrored the trend in initial reactivity towards sulfide: P9-FeOx$_{HYDR}$ (0.59 ± 0.03) > P9-FeOx$_{OXID}$ (0.38) = Fh (0.38 ± 0.11) > Lp (0.24 ± 0.00). The results indicate that any inhibition of Fe reduction and sulfidation by PO_4 surface complexes (Biber et al., 1994) was outweighed by the microscopic (decreased short-range order) and macroscopic (decreased particle size) alterations induced by PO_4 coprecipitation that acted to boost the reactivity of PO_4-bearing FeOx. It appears that PO_4 surface complexes did not interfere with interaction between the solute and the mineral surface, as was the case for dissolved Fe(II). As such, our results show contrasting effects of PO_4 coprecipitation on the extent of FeOx transformation by reaction with dissolved Fe(II) or sulfide.

Dissolved Fe(II) accumulated in high-ΣS(-II) suspensions after depletion of dissolved sulfide, which efficiently scavenges Fe(II) (Fig. 5E, K). Particularly in the case of P9-FeOx$_{HYDR}$, the strong increase in dissolved Fe(II) during the later stages of the experiment indicates ongoing evolution of the reaction products. Specifically, continued electron transport within Fe particles may reduce surface Fe(III) that subsequently detaches as Fe(II)-O bonds are more labile than Fe(III)-O (Dos Santos Afonso and Stumm, 1992; Poulton et al., 2004; Pedersen et al., 2005).

4.5. Release of PO_4 from FeOx upon reaction with dissolved sulfide

Upon exposure to dissolved sulfide, the proportion of FeOx-bound PO_4 that was released into solution was greater than the proportion of sulfidized Fe. In low-ΣS(-II) suspensions, about 5% of Fe was sulfidized but 10–20% of PO_4 was released, even though a significant portion (>60%) of the original FeOx remained. In high-ΣS(-II) suspensions, after 1 h Fe sulfidation and PO_4 release were similar at ~ 60%, in the presence of almost 50% of the original FeOx. The efficient release of PO_4 upon partial sulfidation of FeOx surfaces may reflect a relative enrichment of PO_4 at the surface compared to the bulk mineral, as discussed in Section 4.2. The lack of readsorption of released PO_4 onto the remaining FeOx may be explained by considering the relative abundance of sulfide and FeOx surface sites. In the suspensions, the initial FeOx-Fe(III) concentration was approximately 6 mmol L^{-1}. With estimates of surface site densities of poorly-ordered FeOx in the order of 0.4–0.6 mol/mol Fe (Dzombak and Morel, 1990; Hiemstra, 2013), surface site concentrations were 2–4 mmol L^{-1}. At T_1 (1 h), between 2 and 8 mmol L^{-1} of sulfide was removed from solution in the low- and high-ΣS(-II) suspensions. Therefore, FeOx surface sites may have been occupied by adsorbed sulfide to a large degree, preventing readsorption of PO_4 released during Fe sulfidation. In addition, sulfide may have reacted preferentially with FeOx surface where PO_4 was bound, or adsorption may have displaced some PO_4 from the FeOx surface into solution. Rapid and extensive release of PO_4 from FeOx due to Fe sulfidation in combination with occupation of FeOx surface sites exacerbates the deleterious impact of the onset of sulfidic conditions on the PO_4 retention in soils and sediments.

5. CONCLUSIONS AND IMPLICATIONS

We show that the impact of PO_4 coprecipitation on the structure and short-term fate of Fe(III) precipitation is dependent on the formation pathway of the FeOx and the reactants to which it is exposed. These findings are of interest with regard to Fe cycling and the fate of associated PO_4 in soils and sediments with short-term redox variability (e.g. coastal sediments, salt marshes). Coprecipitation of PO_4 can render poorly-ordered FeOx formed by Fe(III) hydrolysis (Fh) resistant to Fe(II)-catalyzed crystallization and thereby preserve its PO_4 retention capacity. As such, uptake of PO_4 during FeOx formation is a mechanism that sequesters PO_4 and at the same time can increase the stability of this PO_4 sink.

Increased stability is, however, not a general consequence of PO_4 coprecipitation in Fe(III) precipitates. For instance, we observed relatively high rates of dissolved sulfide depletion by PO_4-bearing FeOx, suggesting that increased structural disorder caused by PO_4 coprecipitation may render PO_4-bearing FeOx from Fe(III) hydrolysis more reactive towards sulfide compared to the PO_4-free counterpart (Fh). We attribute this to different reaction mechanisms upon exposure to Fe(II) or sulfide: Fe(II) may be bound to PO_4 complexes on PO_4-bearing FeOx rather than to its surface, thereby inhibiting Fe(II)-Fe(III) electron transfer that initiates Fe(II)-catalyzed FeOx transformation at the mineral surface.

For FeOx formed by Fe(II) oxidation, PO_4 coprecipitation resulted in the formation of a mixture of poorly-ordered P-HFO and poorly-crystalline Lp. The latter was soluble in dilute 0.5 M HCl, in contrast to Lp formed in PO_4-free solutions, highlighting the relatively low stability of this Lp. The relatively disordered and therefore reactive multi-phase Fe(III) precipitate from Fe(II) oxidation in the presence of dissolved PO_4 was more susceptible to both Fe(II)-induced crystallization and sulfidation.

In general, our findings highlight the complexity of predicting the effect of PO_4-induced alterations in short-range structure on the fate and environmental behavior of FeOx and associated nutrients and contaminants. From a geochemical perspective, we note that PO_4-induced changes in FeOx properties can introduce an intricate set of feedbacks, where Fe crystallization and release of associated nutrients and contaminants is initially suppressed under anoxic, non-sulfidic (ferruginous) conditions. However, a (periodic) switch to sulfidic conditions results in accelerated sulfidation and a disproportionate release of nutrients and contaminants. Such environmental feedbacks are relevant for the mobility and bioavailability of essential and toxic elements in a range of settings from aquifers to eutrophic coastal systems.

Declaration of Competing Interest

The authors declare that they have no known competing financial interests or personal relationships that could have appeared to influence the work reported in this paper.

ACKNOWLEDGMENTS

This work was funded by a grant from the Netherlands Organisation for Scientific Research, NWO Veni grant 863.14.014 to P. Kraal. The work was further supported by NWO DUBBLE grant 195.068.1039 for ESRF beamline BM26A. Case M. van Genuchten acknowledges NWO Veni grant 14400. We gratefully thank the technical support and advice of Dipanjan Banerjee at the DUBBLE beamline during Fe K-edge EXAFS data collection. We thank Marcus Ohl and Oliver Plümper at Utrecht University for TEM analysis of P9-FeOx$_{OXID}$. Three anonymous reviewers provided insightful feedback that improved the quality of this article.

APPENDIX A. SUPPLEMENTARY DATA

Supplementary data to this article can be found online at https://doi.org/10.1016/j.gca.2021.12.032.

REFERENCES

Antelo J., Fiol S., Pérez C., Mariño S., Arce F., Gondar D. and López R. (2010) Analysis of phosphate adsorption onto ferrihydrite using the CD-MUSIC model. *J. Colloid Interface Sci.* **347**, 112–119.

APHA (2005) Standard methods for the examination of water and wastewater, 21 ed. American Public Health Association - American Water Works Association - Water Environment Federation.

Bartlett J. K. and Skoog D. A. (1954) Colorimetric determination of elemental sulfur in hydrocarbons. *Anal. Chem.* **26**, 1008–1011.

Biber M. V., dos Santos Afonso M. and Stumm W. (1994) The coordination chemistry of weathering: IV. Inhibition of the dissolution of oxide minerals. *Geochim. Cosmochim. Acta* **58**, 1999–2010.

Borsboom M., Bras W., Cerjak I., Detollenaere D., van Loon D. G., Goedtkind P., Konijnenburg M., Lassing P., Levine Y. K., Munneke B., Oversluizen M., van Tol R. and Vlieg E. (1998) The Dutch-Belgian beamline at the ESRF. *J. Synchrotron Radiat.* **5**, 518–520.

Burdige D. J. (2006) *Geochemistry of marine sediments*. Princeton University Press.

Burton E. D., Sullivan L. A., Bush R. T., Johnston S. G. and Keene A. F. (2008) A simple and inexpensive chromium-reducible sulfur method for acid-sulfate soils. *Appl. Geochem.* **23**, 2759–2766.

Carlson L., Bigham J. M., Schwertmann U., Kyek A. and Wagner F. (2002) Scavenging of as from acid mine drainage by schwertmannite and ferrihydrite: A comparison with synthetic analogues. *Environ. Sci. Technol.* **36**, 1712–1719.

Chupas P. J., Qiu X., Hanson J. C., Lee P. L., Grey C. P. and Billinge S. J. L. (2003) Rapid-acquisition pair distribution function (RA-PDF) analysis. *J. Appl. Crystallogr.* **36**, 1342–1347.

Claff S. R., Sullivan L. A., Burton E. D. and Bush R. T. (2010) A sequential extraction procedure for acid sulfate soils: Partitioning of iron. *Geoderma* **155**, 224–230.

Cline J. D. (1969) Spectrophotometric determination of hydrogen sulfide in natural waters. *Limnol. Oceanogr.* **14**, 454–458.

Cornell R. M. and Giovanoli R. (1988) Acid dissolution of akaganiéite and lepidocrocite: The effect on crystal morphology. *Clays Clay Miner.* **36**, 385–390.

Cornell R. M., Giovanoli R. and Schindler P. W. (1987) Effect of silicate species on the transformation of ferrihydrite into goethite and hematite in alkaline media. *Clays & Clay Minerals* **35**, 21–28.

Cornell R. M. and Schwertmann U. (2003) *The Iron Oxides: Structure, Properties, Reactions, Occurrences and Uses*. Wiley.

Cudennec Y. and Lecerf A. (2005) Topotactic transformations of goethite and lepidocrocite into hematite and maghemite. *Solid State Sci.* **7**, 520–529.

Dos Santos Afonso M. and Stumm W. (1992) Reductive dissolution of iron(III) (hydr)oxides by hydrogen sulfide. *Langmuir* **8**, 1671–1675.

Dzombak D. A. and Morel F. M. M. (1990) *Surface complexation modeling: Hydrous ferric oxide*. Wiley, New York.

Einsele W. (1936) Über die Beziehung des Eisenkreislaufs zum Phosphorkreislauf im eutrophen See. *Arch. Hydrobiol.* **29**, 664–686.

Farrow C. L., Juhas P., Liu J. W., Bryndin D., Božin E. S., Bloch J., Proffen T. and Billinge S. J. L. (2007) PDFfit2 and PDFgui: computer programs for studying nanostructure in crystals. *J. Phys.: Condens. Matter* **19** 335219.

Ferris F. G., Tazaki K. and Fyfe W. S. (1989) Iron oxides in acid mine drainage environments and their association with bacteria. *Chem. Geol.* **74**, 321–330.

Hammersley A. P., Svensson S. O., Hanfland M., Fitch A. N. and Hausermann D. (1996) Two-dimensional detector software: From real detector to idealised image or two-theta scan. *High Pressure Research* **14**, 235–248.

Han X., Tomaszewski E. J., Sorwat J., Pan Y., Kappler A. and Byrne J. M. (2020) Effect of microbial biomass and humic acids on abiotic and biotic magnetite formation. *Environ. Sci. Technol.* **54**, 4121–4130.

Hansel C. M., Benner S. G. and Fendorf S. (2005) Competing Fe (II)-induced mineralization pathways of ferrihydrite. *Environ. Sci. Technol.* **39**, 7147–7153.

Hansel C. M., Benner S. G., Neiss J., Dohnalkova A., Kukkadapu R. K. and Fendorf S. (2003) Secondary mineralization pathways induced by dissimilatory iron reduction of ferrihydrite under advective flow. *Geochim. Cosmochim. Acta* **67**, 2977–2992.

Hellige K., Pollok K., Larese-Casanova P., Behrends T. and Peiffer S. (2012) Pathways of ferrous iron mineral formation upon sulfidation of lepidocrocite surfaces. *Geochim. Cosmochim. Acta* **81**, 69–81.

Hiemstra T. (2013) Surface and mineral structure of ferrihydrite. *Geochim. Cosmochim. Acta* **105**, 316–325.

Hiemstra T. and Van Riemsdijk W. H. (2009) A surface structural model for ferrihydrite I: Sites related to primary charge, molar mass, and mass density. *Geochim. Cosmochim. Acta* **73**, 4423–4436.

Jambor J. L. and Dutrizac J. E. (1998) Occurrence and constitution of natural and synthetic ferrihydrite, a widespread iron oxyhydroxide. *Chem. Rev.* **98**, 2549–2586.

Jensen H. S., Kristensen P., Jeppesen E. and Skytthe A. (1992) Iron-phosphorus ratio in surface sediment as an indicator of phosphate release from aerobic sediments in shallow lakes. *Hydrobiologia* **235**, 731–743.

Kaegi R., Voegelin A., Folini D. and Hug S. J. (2010) Effect of phosphate, silicate, and Ca on the morphology, structure and elemental composition of Fe(III)-precipitates formed in aerated Fe(II) and As(III) containing water. *Geochim. Cosmochim. Acta* **74**, 5798–5816.

Karlsson T. and Persson P. (2010) Coordination chemistry and hydrolysis of Fe(III) in a peat humic acid studied by X-ray absorption spectroscopy. *Geochim. Cosmochim. Acta* **74**, 30–40.

Kelly S. D., Hesterberg D. and Ravel B. (2008) Analysis of soils and minerals using X-ray absorption spectroscopy. In *Methods of Soil Analysis Part 5—Mineralogical Methods* (eds. A. L. Ulery and L. R. Drees). Soil Science Society of America, Madison, Wisconsin.

Khare N., Hesterberg D., Beauchemin S. and Wang S.-L. (2004) XANES determination of adsorbed phosphate distribution between ferrihydrite and boehmite in mixtures. *Soil Sci. Soc. Am. J.* **68**, 460–469.

Kim J., Li W., Philips B. L. and Grey C. P. (2011) Phosphate adsorption on the iron oxyhydroxides goethite (α-FeOOH), akaganeite (β-FeOOH), and lepidocrocite (γ-FeOOH): a 31P NMR study. *Energy & Environ. Sci.* **4**, 4298–4305.

Kraal P., Burton E. D. and Bush R. T. (2013) Iron monosulfide accumulation and pyrite formation in eutrophic estuarine sediments. *Geochim. Cosmochim. Acta* **122**, 75–88.

Kraal P., Dijkstra N., Behrends T. and Slomp C. P. (2017) Phosphorus burial in sediments of the sulfidic deep Black Sea: key roles for adsorption by calcium carbonate and apatite authigenesis. *Geochim. Cosmochim. Acta* **204**, 140–158.

Kraal P., van Genuchten C. M., Behrends T. and Rose A. L. (2019) Sorption of phosphate and silicate alters dissolution kinetics of poorly crystalline iron (oxyhydr)oxide. *Chemosphere* **234**, 690–701.

Kraal P., van Genuchten C. M., Lenstra W. K. and Behrends T. (2020) Coprecipitation of phosphate and silicate affects environmental iron (oxyhydr)oxide transformations: A gel-based diffusive sampler approach. *Environ. Sci. Technol.* **54**, 12795–12802.

Krom M. D. and Berner R. A. (1980) Adsorption of phosphate in anoxic marine sediments. *Limnol. Oceanogr.* **25**, 797–806.

Majzlan J. (2011) Thermodynamic stabilization of hydrous ferric oxide by adsorption of phosphate and arsenate. *Environ. Sci. Technol.* **45**, 4726–4732.

Manceau A. and Drits V. A. (1993) Local structure of ferrihydrite and feroxyhite by exafs spectroscopy. *Clay Miner.* **28**, 165–184.

Michel F. M., Ehm L., Antao S. M., Lee P. L., Chupas P. J., Liu G., Strongin D. R., Schoonen M. A. A., Phillips B. L. and Parise J. B. (2007) The structure of ferrihydrite, a nanocrystalline material. *Science* **316**, 1726–1729.

Mortimer C. H. (1941) The exchange of dissolved substances between mud and water. *J. Ecology* **29**, 280–329.

Nikitenko S., Beale A. M., van der Eerden A. M. J., Jacques S. D. M., Leynaud O., O'Brien M. G., Detollenaere D., Kaptein R., Weckhuysen B. M. and Bras W. (2008) Implementation of a combined SAXS/WAXS/QEXAFS set-up for time-resolved in situ experiments. *J. Synchrotron Radiat.* **15**, 632–640.

Nixon S. W. (1995) Coastal marine eutrophication: A definition, social causes, and future concerns. *Ophelia* **41**, 199–219.

O'Day P. A., Rivera N., Root R. and Carroll S. A. (2004) X-ray absorption spectroscopic study of Fe reference compounds for the analysis of natural sediments. *Am. Mineral.* **89**, 572–585.

Paige C. R., Snodgrass W. J., Nicholson R. V., Scharer J. M. and He Q. H. (1997) The effect of phosphate on the transformation of ferrihydrite into crystalline products in alkaline media. *Water, Air, & Soil Pollution* **97**, 397–412.

Pedersen H. D., Postma D., Jakobsen R. and Larsen O. (2005) Fast transformation of iron oxyhydroxides by the catalytic action of aqueous Fe(II). *Geochim. Cosmochim. Acta* **69**, 3967–3977.

Peiffer S., Behrends T., Hellige K., Larese-Casanova P., Wan M. and Pollok K. (2015) Pyrite formation and mineral transformation pathways upon sulfidation of ferric hydroxides depend on mineral type and sulfide concentration. *Chem. Geol.* **400**, 44–55.

Peiffer S. and Wan M. (2016) Reductive dissolution and reactivity of ferric (hydr)oxides: New insights and implications for environmental redox processes, iron oxides. *Wiley-VCH Verlag GmbH & Co. KGaA*, 31–52.

Pokrovski G. S., Schott J., Farges F. and Hazemann J.-L. (2003) Iron (III)-silica interactions in aqueous solution: insights from X-ray absorption fine structure spectroscopy. *Geochim. Cosmochim. Acta* **67**, 3559–3573.

Poulton S. W., Krom M. D. and Raiswell R. (2004) A revised scheme for the reactivity of iron (oxyhydr)oxide minerals towards dissolved sulfide. *Geochim. Cosmochim. Acta* **68**, 3703–3715.

Queiroz H. M., Ferreira T. O., Barcellos D., Nóbrega G. N., Antelo J., Otero X. L. and Bernardino A. F. (2021) From sinks to sources: The role of Fe oxyhydroxide transformations on phosphorus dynamics in estuarine soils. *J. Environ. Manage.* **278** 111575.

Raiswell R. and Canfield D. E. (1998) Sources of iron for pyrite formation in marine sediments. *Am. J. Sci.* **298**, 219–245.

Ravel B. and Newville M. (2005) Athena, artemis, hephaestus: data analysis for X-ray absorption spectroscopy using IFEFFIT. *J. Synchrotron Radiat.* **12**, 537–541.

Ren Y., Shui H., Peng C., Liu H. and Hu Y. (2011) Solubility of elemental sulfur in pure organic solvents and organic solvent–ionic liquid mixtures from 293.15 to 353.15K. *Fluid Phase Equilib.* **312**, 31–36.

Rickard D. and Morse J. W. (2005) Acid volatile sulfide (AVS). *Mar. Chem.* **97**, 141–197.

Rickard D. T. (1975) Kinetics and mechanism of pyrite formation at low temperatures. *Am. J. Sci.* **275**, 636–652.

Rose J., Manceau A., Bottero J.-Y., Masion A. and Garcia F. (1996) Nucleation and growth mechanisms of Fe oxyhydroxide in the presence of PO_4 ions. 1. Fe K-Edge EXAFS study. *Langmuir* **12**, 6701–6707.

Rossberg A., Reich T. and Bernhard G. (2003) Complexation of uranium(VI) with protocatechuic acid—application of iterative transformation factor analysis to EXAFS spectroscopy. *Anal. Bioanal. Chem.* **376**, 631–638.

Rothe M., Kleeberg A. and Hupfer M. (2016) The occurrence, identification and environmental relevance of vivianite in waterlogged soils and aquatic sediments. *Earth-Sci. Rev.* **158**, 51–64.

Ruttenberg K. C. (2014) The global phosphorus cycle. In *Treatise on Geochemistry* (eds. H. D. Holland and K. K. Turekian), second ed. Elsevier, Oxford, pp. 499–558.

Schwertmann U. (1988) Occurrence and formation of iron oxides in various pedoenvironments. In *Iron in Soils and Clay Minerals* (eds. J. W. Stucki, B. A. Goodman and U. Schwertmann). Springer, Netherlands, Dordrecht, pp. 267–308.

Schwertmann U. and Cornell S. (1991) *Iron oxides in the laboratory: Preparation and characterization*. Wiley.

Schwertmann U. and Taylor R. M. (1972) The transformation of lepidocrocite to goethite. *Clays Clay Miner.* **20**, 151–158.

Senn A.-C., Hug S. J., Kaegi R., Hering J. G. and Voegelin A. (2018) Arsenate co-precipitation with Fe(II) oxidation products and retention or release during precipitate aging. *Water Res.* **131**, 334–345.

Senn A.-C., Kaegi R., Hug S. J., Hering J. G., Mangold S. and Voegelin A. (2015) Composition and structure of Fe(III)-precipitates formed by Fe(II) oxidation in water at near-neutral pH: Interdependent effects of phosphate, silicate and Ca. *Geochim. Cosmochim. Acta* **162**, 220–246.

Senn A.-C., Kaegi R., Hug S. J., Hering J. G., Mangold S. and Voegelin A. (2017) Effect of aging on the structure and phosphate retention of Fe(III)-precipitates formed by Fe(II) oxidation in water. *Geochim. Cosmochim. Acta* **202**, 341–360.

Sherman D. M. (1987) Molecular orbital (SCF-Xα-SW) theory of metal-metal charge transfer processes in minerals. I. Application to $Fe^{2+} \rightarrow Fe^{3+}$ charge transfer and "electron delocalization" in mixed-valence iron oxides and silicates. *Phys. Chem. Miner.* **14**, 355–363.

Sleiman N., Deluchat V., Wazne M., Courtin A., Saad Z., Kazpard V. and Baudu M. (2016) Role of iron oxidation byproducts in the removal of phosphate from aqueous solution. *RSC Adv.* **6**, 1627–1636.

Smith V. H., Tilman G. D. and Nekola J. C. (1999) Eutrophication: impacts of excess nutrient inputs on freshwater, marine, and terrestrial ecosystems. *Environ. Pollut.* **100**, 179–196.

Thompson J., Poulton S. W., Guilbaud R., Doyle K. A., Reid S. and Krom M. D. (2019) Development of a modified SEDEX phosphorus speciation method for ancient rocks and modern iron-rich sediments. *Chem. Geol.*.

Tronc E., Belleville P., Jolivet J. P. and Livage J. (1992) Transformation of ferric hydroxide into spinel by iron(II) adsorption. *Langmuir* **8**, 313–319.

van der Grift B., Behrends T., Osté L. A., Schot P. P., Wassen M. J. and Griffioen J. (2016) Fe hydroxyphosphate precipitation and Fe(II) oxidation kinetics upon aeration of Fe(II) and phosphate-containing synthetic and natural solutions. *Geochim. Cosmochim. Acta* **186**, 71–90.

van Genuchten C. M., Gadgil A. J. and Peña J. (2014a) Fe(III) nucleation in the presence of bivalent cations and oxyanions leads to subnanoscale 7 Å polymers. *Environ. Sci. Technol.* **48**, 11828–11836.

van Genuchten C. M., Peña J., Amrose S. E. and Gadgil A. J. (2014b) Structure of Fe(III) precipitates generated by the electrolytic dissolution of Fe(0) in the presence of groundwater ions. *Geochim. Cosmochim. Acta* **127**, 285–304.

Voegelin A., Kaegi R., Frommer J., Vantelon D. and Hug S. J. (2010) Effect of phosphate, silicate, and Ca on Fe(III)-precipitates formed in aerated Fe(II)- and As(III)-containing water studied by X-ray absorption spectroscopy. *Geochim. Cosmochim. Acta* **74**, 164–186.

Voegelin A., Senn A.-C., Kaegi R., Hug S. J. and Mangold S. (2013) Dynamic Fe-precipitate formation induced by Fe(II) oxidation in aerated phosphate-containing water. *Geochim. Cosmochim. Acta* **117**, 216–231.

Wan M., Schröder C. and Peiffer S. (2017) Fe(III):S(-II) concentration ratio controls the pathway and the kinetics of pyrite formation during sulfidation of ferric hydroxides. *Geochim. Cosmochim. Acta* **217**, 334–348.

Waychunas G. A., Rea B. A., Fuller C. C. and Davis J. A. (1993) Surface chemistry of ferrihydrite: Part 1. EXAFS studies of the geometry of coprecipitated and adsorbed arsenate. *Geochim. Cosmochim. Acta* **57**, 2251–2269.

Yan W., Liu H., Chen R., Xie J. and Wei Y. (2015) Dissolution and oriented aggregation: transformation from lepidorocite to goethite by the catalysis of aqueous Fe(ii). *RSC Adv.* **5**, 106396–106399.

Yang L., Steefel C. I., Marcus M. A. and Bargar J. R. (2010) Kinetics of Fe(II)-catalyzed transformation of 6-line ferrihydrite under anaerobic flow conditions. *Environ. Sci. Technol.* **44**, 5469–5475.

Associate editor: Owen Duckworth